Commun. Comput. Phys.
doi: 10.4208/cicp.OA-2021-0126

Vol. **31**, No. 3, pp. 771-815
March 2022

High-Order Positivity-Preserving Well-Balanced Discontinuous Galerkin Methods for Euler Equations with Gravitation on Unstructured Meshes

Weijie Zhang[1,2], Yulong Xing[2], Yinhua Xia[1] and Yan Xu[1,*]

[1] *School of Mathematical Sciences, University of Science and Technology of China, Hefei, Anhui 230026, P.R. China.*
[2] *Department of Mathematics, The Ohio State University, Columbus, OH 43210, USA.*

Received 10 June 2021; Accepted (in revised version) 19 October 2021

Abstract. In this paper, we propose a high-order accurate discontinuous Galerkin (DG) method for the compressible Euler equations under gravitational fields on unstructured meshes. The scheme preserves a general hydrostatic equilibrium state and provably guarantees the positivity of density and pressure at the same time. Comparing with the work on the well-balanced scheme for Euler equations with gravitation on rectangular meshes, the extension to triangular meshes is conceptually plausible but highly nontrivial. We first introduce a special way to recover the equilibrium state and then design a group of novel variables at the interface of two adjacent cells, which plays an important role in the well-balanced and positivity-preserving properties. One main challenge is that the well-balanced schemes may not have the weak positivity property. In order to achieve the well-balanced and positivity-preserving properties simultaneously while maintaining high-order accuracy, we carefully design DG spatial discretization with well-balanced numerical fluxes and suitable source term approximation. For the ideal gas, we prove that the resulting well-balanced scheme, coupled with strong stability preserving time discretizations, satisfies a weak positivity property. A simple existing limiter can be applied to enforce the positivity-preserving property, without losing high-order accuracy and conservation. Extensive one- and two-dimensional numerical examples demonstrate the desired properties of the proposed scheme, as well as its high resolution and robustness.

AMS subject classifications: 65M60, 35L60, 35L65, 65M12

Key words: Discontinuous Galerkin methods, Euler equations, gravitational field, positivity-preserving, well-balanced, triangular mesh.

*Corresponding author. *Email addresses:* zhwj@mail.ustc.edu.cn (W. Zhang), xing.205@osu.edu (Y. Xing), yhxia@ustc.edu.cn (Y. Xia), yxu@ustc.edu.cn (Y. Xu)

1 Introduction

In this paper, we develop high-order accurate positivity-preserving well-balanced discontinuous Galerkin (DG) methods for the compressible Euler equations with gravitation on unstructured meshes. This model has many interesting astrophysical and atmospheric applications, and takes the form

$$\boldsymbol{U}_t+\nabla\cdot\boldsymbol{F}(\boldsymbol{U})=\boldsymbol{S}(\boldsymbol{U},\nabla\phi), \tag{1.1}$$

in the d-dimensional case, with

$$\boldsymbol{U}=\begin{pmatrix}\rho\\ \boldsymbol{m}\\ E\end{pmatrix},\quad \boldsymbol{F}(\boldsymbol{U})=\begin{pmatrix}\rho\boldsymbol{u}\\ \rho\boldsymbol{u}\otimes\boldsymbol{u}+p\boldsymbol{I}_d\\ (E+p)\boldsymbol{u}\end{pmatrix},\quad \boldsymbol{S}(\boldsymbol{U},\nabla\phi)=\begin{pmatrix}0\\ -\rho\nabla\phi\\ -\boldsymbol{m}\cdot\nabla\phi\end{pmatrix}, \tag{1.2}$$

where $\boldsymbol{m}=\rho\boldsymbol{u}$ denotes the momentum vector; $\rho,\boldsymbol{u},p$ denote the fluid density, velocity and pressure; $\boldsymbol{I}_d$ is the identity matrix of size d; $E=\frac{1}{2}\rho\|\boldsymbol{u}\|^2+\rho e$ (e is specific internal energy) is the non-gravitational energy; $\phi(\boldsymbol{x})$ is the time independent gravitational potential. The pressure p is linked to the density ρ and the internal energy e. In this paper, we consider the ideal gas with the following equation of state

$$p=(\gamma-1)\rho e=(\gamma-1)\left(E-\frac{\|\boldsymbol{m}\|^2}{2\rho}\right), \tag{1.3}$$

where γ is the ratio of specific heats.

The Euler equations under gravitation fields admit hydrostatic equilibrium solutions, in which the gravitational source term is exactly balanced by the flux gradient. Two well-known hydrostatic equilibrium states are the isothermal and the polytropic equilibria. For these hyperbolic balance laws, the well-balanced schemes are introduced to exactly preserve the equilibrium states at a discrete level. An important advantage of the well-balanced schemes is that they can effectively and accurately resolve the nearly equilibrium flows on relatively coarse meshes. These nearly equilibrium flows are small perturbation of the hydrostatic equilibrium states, and often appear in the astrophysical and atmospheric applications. Well-balanced methods for the shallow water equations with source term have been extensively studied in the past few decades, see [1,4,7,18,21, 29,42,44] and the review papers [28,46]. Recently, research on well-balanced schemes for the Euler equations with gravitation has attracted much attention. Such method was first studied by LeVeque and Bale [30] based on the quasi-steady wave propagation methods designed for the shallow water equations. After that, extensive well-balanced methods for the Euler equations with gravitation have been designed and studied within the framework of finite volume [2,3,5,8,9,11,17,22,25,27,31,38], finite difference [19,26,33,45], finite element discontinuous Galerkin (DG) [10, 32, 34, 39] and gas-kinetic schemes [47], and both first order and high order methods have been investigated. Recently, there are increasing interests in designing well-balanced methods for general equilibrium state.

In [27,39], well-balanced methods for moving equilibrium states of Euler equations with gravity are studied based on explicitly given equilibria. The well-balanced methods requiring no a-priori knowledge of the equilibrium were also studied in [3, 17, 26, 35]. In [39], the comparison of numerical performance of high order DG and well-balanced DG methods is studied, which demonstrated the advantage of well-balanced methods in multi-dimensional applications.

Another well-known numerical challenge in the numerical simulation of the Euler equation appear when the density and/or pressure is small. Physically, both the density and the pressure should stay positive, however, this may not be preserved numerically, and the appearance of negative density or pressure may cause the breakdown of the numerical simulations. Most commonly used high order numerical schemes for solving hyperbolic conservation laws do not in general preserve the positivity of these quantities automatically, and there have been many studies on the design of high order bound-preserving numerical schemes for conservation laws, including the Euler equations. We refer to the recent articles [23,24,36] and the references therein for the recent development and discussion along this direction. Among these approaches, one idea is to utilize a simple scaling limiter [48], which maintains the local conservation and high order accuracy of the original method. This technique has been used to design high-order positivity-preserving DG schemes for Euler equations without source term [48] and with source terms [49].

The high order finite element DG method will be considered in this paper. It is a popular high-order method for solving hyperbolic conservation laws. The Runge-Kutta DG methods have been analyzed by Cockburn, Shu et al. in a series of papers, e.g. [12–16], and have been successfully utilized in a wide range of applications. There have been two approaches in the DG framework to obtain well-balanced property for the Euler equations with gravity. The first approach is based on the reformulation of the source term technique originally proposed for the shallow water equations in [43], and later applied to the Euler equations in [10,19,31,32,45]. Recently, a positivity-preserving well-balanced DG scheme has been developed in [40] for the Euler equations with gravity. The well-balanced idea therein was adopted from this type of approach studied in [32], with a properly modified Harten-Lax-van Leer-contact (HLLC) flux. Rigorous positivity-preserving analyses are carried out based on some technical decompositions as well as several key properties of the admissible states and HLLC flux. It was demonstrated that a simple existing rescaling limiter can be used to effectively enforce the positivity-preserving property, without losing high-order accuracy and conservation. The other approach to achieve well-balanced property is to decompose the solution into equilibrium and non-equilibrium components, and then utilize the hydrostatic reconstruction idea originally proposed in [1] and widely studied for the shallow water equations. The well-balanced DG scheme based on the generalized hydrostatic reconstruction technique has been developed for the Euler equations in [34] to preserve the isothermal and polytropic equilibrium states.

In this paper, we propose to develop high-order positivity-preserving well-balanced

DG schemes for the Euler equations with gravitation on unstructured meshes. The objectives of this paper are threefold. First, the well-balanced technique to be introduced is built upon and improves the one studied in [34]. We have found out that, although the accuracy test carried out in [34] demonstrated the optimal convergence rate of the proposed well-balanced DG method, some extra tests with manufactured solutions suggest that suboptimal convergence rate could be observed numerically. Therefore, we propose an improvement of the source term approximation to ensure optimal convergence for all the numerical tests we tried. In addition, we note that our proposed well-balanced methods don't need to assume an explicitly given equilibrium state, but only the a-priori knowledge of it. Second, in order to achieve the well-balanced and positivity-preserving properties simultaneously while maintaining high-order accuracy, we carefully design DG spatial discretization, and prove that the resulting well-balanced scheme, coupled with strong stability preserving time discretizations, satisfies a weak positivity property. The same simple existing limiter in [40] can be applied to enforce the positivity-preserving property. We would like to remark that the rigorous proof of the weak positivity property is very different from the one in [40], which could be useful for other applications. Last, most of the works on well-balanced methods for Euler equations are introduced in one dimension and two dimensions on rectangular meshes. In this paper, the unstructured triangular meshes will be considered, which brings additional challenge in the design of well-balanced methods.

The rest of this paper is organized as follows. In Section 2, we introduce the hydrostatic equilibrium states and some necessary notations for DG methods. The well-balanced DG methods for the Euler equations with gravitation are presented in Section 3. In Section 4, we show that our scheme has a weak positivity property, and a simple scaling limiter can be applied to preserve the positivity of density and the pressure under suitable time step. In Section 5, we provide numerical examples both for the isothermal and polytropic equilibrium states to verify the well-balanced property, high-order accuracy and positivity-preserving property in one dimension and two dimensions on triangular meshes. Finally, we will give some concluding remarks in Section 6. In Appendix A and B, we show proofs in Section 4 that are too long in the article to increase readability.

2 Mathematical model and notations

This section introduces the hydrostatic equilibrium states of (1.1), the admissible state set and some necessary notations of the DG methods.

2.1 Hydrostatic equilibrium states

The model (1.1) admits the hydrostatic equilibrium states of the form

$$\rho=\rho(\boldsymbol{x}),\quad \boldsymbol{u}=0,\quad \nabla p=-\rho\nabla\phi, \tag{2.1}$$

where $\boldsymbol{x}\in\mathbb{R}^d$ is the spatial variables. Two important equilibria arising in the applications are the polytropic [25] and isothermal [41] hydrostatic states.

An ideal gas satisfies

$$p(\boldsymbol{x})=\rho(\boldsymbol{x})RT(\boldsymbol{x}), \tag{2.2}$$

with R being the universal gas constant. If the temperature $T(x)\equiv T_0$ becomes a constant, we have the following isothermal equilibrium state

$$\rho=\rho_0\exp\left(-\frac{\phi}{RT_0}\right),\quad \boldsymbol{u}=0,\quad p=p_0\exp\left(-\frac{\phi}{RT_0}\right), \tag{2.3}$$

with $p_0=\rho_0RT_0$.

The other polytropic hydrostatic equilibrium is characterized by

$$p=\kappa_0\rho^\gamma, \tag{2.4}$$

which will lead to the form of

$$\rho=\left(\frac{\gamma-1}{\kappa_0\gamma}(C-\phi)\right)^{\frac{1}{\gamma-1}},\quad \boldsymbol{u}=0,\quad p=\kappa_0^{\frac{1}{1-\gamma}}\left(\frac{\gamma-1}{\gamma}(C-\phi)\right)^{\frac{\gamma}{\gamma-1}}, \tag{2.5}$$

where C and κ_0 are both constants. An equivalent formulation is given by

$$\boldsymbol{u}=0,\quad h+\phi=C, \tag{2.6}$$

with $h=e+\frac{p}{\rho}$ being the specific enthalpy.

2.2 The admissible state

Physically, both the density ρ and the pressure p stay positive, therefore we can define the physically admissible states

$$G:=\left\{\boldsymbol{U}=(\rho,\boldsymbol{m},E)^T\;\middle|\;\rho>0,\ \mathcal{G}(\boldsymbol{U}):=E-\frac{\|\boldsymbol{m}\|^2}{2\rho}>0\right\}, \tag{2.7}$$

where the condition $\mathcal{G}(\boldsymbol{U})>0$ is equivalent to the fact that the pressure p is positive.

2.3 Notations

We assume that the computational domain $\Omega\in\mathbb{R}^d$ is partitioned into an unstructured mesh $\mathcal{T}$, such that

$$\Omega=\bigcup\{K\mid K\in\mathcal{T}\},$$

and we denote the volume of cell K by Δ_K. The $d+1$ vertices of each cell $K\in\mathcal{T}$ are denoted by $\boldsymbol{x}_{K,1},\cdots,\boldsymbol{x}_{K,d+1}$. We denote the cell boundary of the element K by

$$\partial K:=\bigcup_{\nu=1}^{d+1}F_K^\nu, \tag{2.8}$$

where F_K^ν, $\nu=1,\cdots,d+1$, are edges of K. We also denote the length of F_K^ν by $|F_K^\nu|$ and the outward unit normal vector of K with respect to the edge F_K^ν by $\boldsymbol{n}_K^\nu$.

The finite element space of discontinuous piecewise polynomial functions is defined as

$$\mathcal{V}^k := \left\{ \varphi(\boldsymbol{x}) \in L^2(\Omega) \;\middle|\; \varphi(\boldsymbol{x})|_K \in \mathbb{P}^k(K),\ \forall K \in \mathcal{T} \right\}, \tag{2.9}$$

where $\mathbb{P}^k(K)$ is the space of polynomials with total degree up to k in cell K. For the system of Euler equations, we define the finite element space

$$\boldsymbol{\Pi}_d^k := \left\{ (\varphi_1,\cdots,\varphi_{d+2})^T | \varphi_i \in \mathcal{V}^k, \text{for } i=1,\cdots,d+2 \right\}, \tag{2.10}$$

which consists of $d+2$ components in the d-dimensional setting.

Since the values of $\varphi \in \mathcal{V}^k$ can be discontinuous on the interface of two adjacent cells, we define the limits at the cell boundary ∂K as

$$\varphi^{int_K}(\boldsymbol{x}) := \lim_{\epsilon\to 0^+} \varphi(\boldsymbol{x}-\epsilon \boldsymbol{n}_K^\nu), \quad \varphi^{ext_K}(\boldsymbol{x}) := \lim_{\epsilon\to 0^+} \varphi(\boldsymbol{x}+\epsilon \boldsymbol{n}_K^\nu), \quad \forall \boldsymbol{x} \in F_K^\nu.$$

With an abuse of notation, we denote the numerical solution by $\boldsymbol{U}$. The standard semi-discrete DG methods for (1.1) are given as follow: for any test function $\boldsymbol{\varphi} \in \boldsymbol{\Pi}_d^k$, find $\boldsymbol{U} \in \boldsymbol{\Pi}_d^k$, such that

$$\frac{\mathrm{d}}{\mathrm{d}t}\int_K \boldsymbol{U}\cdot\boldsymbol{\varphi}\mathrm{d}\boldsymbol{x} = \int_K \boldsymbol{F}(\boldsymbol{U}) : \nabla\boldsymbol{\varphi}\mathrm{d}\boldsymbol{x} - \int_{\partial K} \hat{\boldsymbol{F}}\left(\boldsymbol{U}^{int_K}, \boldsymbol{U}^{ext_K}, \boldsymbol{n}\right)\cdot\boldsymbol{\varphi}\mathrm{d}\boldsymbol{s} + \int_K \boldsymbol{S}(\boldsymbol{U},\nabla\phi)\cdot\boldsymbol{\varphi}\mathrm{d}\boldsymbol{x}, \tag{2.11}$$

where we employ the notation $:$ such that $A:B=\sum_{i,j} a_{ij}b_{ij}$ for any matrices $A=\left[a_{ij}\right]$ and $B=\left[b_{ij}\right] \in \mathbb{R}^{n\times m}$. $\hat{\boldsymbol{F}}$ denotes the numerical flux, and the simple Lax-Friedrichs (LF) numerical flux

$$\hat{\boldsymbol{F}}\left(\boldsymbol{U}^{int}, \boldsymbol{U}^{ext}, \boldsymbol{n}\right) := \frac{1}{2}\left(\boldsymbol{F}\left(\boldsymbol{U}^{int}\right)\cdot\boldsymbol{n} + \boldsymbol{F}\left(\boldsymbol{U}^{ext}\right)\cdot\boldsymbol{n} - \alpha\left(\boldsymbol{U}^{ext}-\boldsymbol{U}^{int}\right)\right), \tag{2.12}$$

is used in this paper, where

$$\alpha = \max_{\boldsymbol{U}\in\{\boldsymbol{U}^{int},\boldsymbol{U}^{ext}\}} \left(|\boldsymbol{u}\cdot\boldsymbol{n}| + \sqrt{\gamma p/\rho}\right). \tag{2.13}$$

3 The well-balanced DG methods

In this section, we present the well-balanced DG methods for the Euler equations with gravitation. The proposed methods are established on triangular meshes, extending the result in [34].

3.1 Recovery of equilibrium states

We begin with the recovery of equilibrium states in the design of well-balanced methods. At each time step, the equilibrium state will be recovered from the numerical solution $\boldsymbol{U}$. One useful tool is a projection into the DG space while matching the value at the cell interface, presented in [6,34] for the one-dimensional (1D) case and two-dimensional (2D) case with rectangular mesh. We refer to [34] for the detailed discussion and motivation of such projection. For unstructured meshes, the same projection is no longer applicable and a different projection will be defined below to achieve our goal.

One hopes that this projection can keep the function value unchanged at the boundary of the cell K, and then we can recover a reference equilibrium state from the numerical solution with the aid of the unchanged point values. There are many high-order projections that meet this goal and we choose the continuous finite element projection to simplify the well-balanced procedure. We note that although the continuous finite element projection is used, our proposed scheme is based on DG methods and the projection is used for the initialization and recovery of equilibrium states only.

For any function $\varphi \in L^2(\Omega)$, the projection $\mathcal{P}^k\varphi$ utilized in this paper is given as follows:

$$\mathcal{P}^k\varphi(\boldsymbol{x}_{K,i}) = \varphi(\boldsymbol{x}_{K,i}), \tag{3.1}$$

for any point $\{\boldsymbol{x}_{K,i}\}_{i=1}^b$ in the given cell K, with $b = \frac{(k+d)!}{k!d!}$ denoting the dimension of d-dimensional space $\mathbb{P}^k$. For one dimensional case, the points $\{\boldsymbol{x}_{K,i}\}_{i=1}^b$ uniformly distribute over the entire cell K containing the two endpoints. For the cases of $k=1,2,3$, these points are the black solid dots in Fig. 1, and similar case for higher-order polynomials can be derived. For two dimensional case, there are $k+1$ uniformly distributed points on each triangle face F_K^v including the vertices of cell K, and other points, if existed, locates in the interior of the element K. For the cases of $k=1,2,3$, these points are the black solid dots in Fig. 2, and similar case for higher-order polynomials can be derived. We define the numerical initial condition of the DG methods as

$$\boldsymbol{U}^0 = \mathcal{P}^k\boldsymbol{U}_{ex}(\boldsymbol{x},0), \tag{3.2}$$

and note that these two functions share the same function values at the points $\{\boldsymbol{x}_{K,i}\}_{i=1}^b$.

Another important component in the design of well-balanced methods is the introduction of a "local" reference equilibrium state, denoted by $\boldsymbol{U}^r$, which will be computed at each time step following the procedure outlined below. The goal is to recover the targeting (isothermal or polytropic) equilibrium, i.e., $\boldsymbol{U}^r = \boldsymbol{U}_{eq}$, when the numerical so-

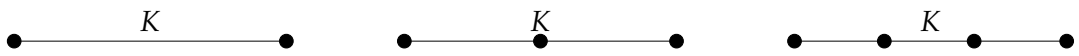

Figure 1: The points $\{\boldsymbol{x}_{K,i}\}_{i=1}^b$ in the cell K are denoted by the black solid dots for one-dimensional case. From left to right: the case of $k=1,2,3$ with k being the polynomial degree.

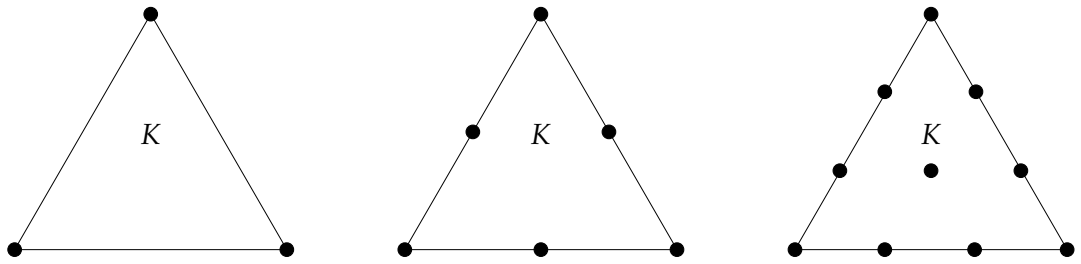

Figure 2: The points $\{\boldsymbol{x}_{K,i}\}_{i=1}^{b}$ in the cell K are denoted by the black solid dots for two-dimensional case. From left to right: the case of $k=1,2,3$ with k being the polynomial degree.

lution reaches the equilibrium state (i.e., $\boldsymbol{U}^n=\mathcal{P}^k\boldsymbol{U}_{eq}$ for some n with the same projection $\mathcal{P}^k$ defined above). The first step is to pick one point (denoted by $\boldsymbol{x}_0$) from the set $\{\boldsymbol{x}_{K,i}\}_{i=1}^{b}$. In our numerical implementation, we choose the right endpoint of the cell for one-dimensional case and the point $\boldsymbol{x}_{K,1}$ for two-dimensional case. Then the reference equilibrium state $\boldsymbol{U}_K^r=(\rho_K^r,\boldsymbol{m}_K^r,E_K^r)^T$ in each cell K is constructed as follows.

- For the isothermal equilibrium

$$\rho_K^r=\exp\left(\frac{C_1-\phi}{RT_0}\right),\quad \boldsymbol{u}_K^r=0,\quad p_K^r=RT_0\exp\left(\frac{C_1-\phi}{RT_0}\right), \tag{3.3}$$

  where

$$T_0=\frac{p_K(\boldsymbol{x}_0)}{R\rho_K(\boldsymbol{x}_0)},\quad C_1=T_0\log\rho_K(\boldsymbol{x}_0)+\phi_K(\boldsymbol{x}_0). \tag{3.4}$$

- For the polytropic equilibrium

$$\rho_K^r=\left(\frac{\gamma-1}{\kappa\gamma}(C_2-\phi)\right)^{\frac{1}{\gamma-1}},\quad \boldsymbol{u}_K^r=0,\quad p_K^r=\kappa^{\frac{1}{1-\gamma}}\left(\frac{\gamma-1}{\gamma}(C_2-\phi)\right)^{\frac{\gamma}{\gamma-1}}, \tag{3.5}$$

  where

$$C_2=\frac{\gamma p_K(\boldsymbol{x}_0)}{(\gamma-1)\rho_K(\boldsymbol{x}_0)}+\phi_K(\boldsymbol{x}_0),\quad \kappa=\frac{p_K(\boldsymbol{x}_0)}{(\rho_K(\boldsymbol{x}_0))^\gamma}. \tag{3.6}$$

Here $\boldsymbol{U}_K=(\rho_K,\boldsymbol{m}_K,E_K)^T$ denotes the numerical solution in the cell K. If other type of equilibrium state is reached, similar approach can be used to construct $\boldsymbol{U}_K^r$.

Remark 3.1. We note that our selected projection (3.1) is similar with the work in the nodal DG framework [10], as one of the motivations is to ensure that the projection is continuous on the cell boundaries so that the consistency of the numerical flux can be used at the equilibrium state. One of the difference of these two works is that our approach is designed on unstructured triangular meshes and the Gauss–Lobatto–Legendre points cannot maintain high-order accuracy and continuity on cell boundaries at the

same time. Also, our work involves the recovery of equilibrium states, which leads to different source term approximations. Such approach can aid in the positivity-preserving property, which will be introduced in Section 4.

3.2 The well-balanced modification

The standard DG methods (2.11) may not be able to preserve the equilibrium state automatically, and we will discuss the modification to achieve well-balanced property. We follow the well-balanced approaches in [34], and take in consideration the additional challenge due to the unstructured mesh and the compatibility with the positivity-preserving issue. We will introduce a series of boundary modifications and corresponding source term approximation in this section and prove the weak positivity property in the next section.

3.2.1 Decomposition

We first decompose the numerical solution $\boldsymbol{U}$ into two parts:

$$\boldsymbol{U}^e=\mathcal{P}^k\boldsymbol{U}^r,\quad \boldsymbol{U}^f=\boldsymbol{U}-\boldsymbol{U}^e, \tag{3.7}$$

where $\boldsymbol{U}^r$ is the "local" reference equilibrium state introduced in Section 3.1. In this decomposition, $\boldsymbol{U}^e$ stands for the equilibrium component and $\boldsymbol{U}^f$ denotes the fluctuation component. Note that $\boldsymbol{U}^e$ and $\boldsymbol{U}^f$ both belong to $\boldsymbol{\Pi}_d^k$ while $\boldsymbol{U}^r\notin\boldsymbol{\Pi}_d^k$. Moreover, if the initial condition $\boldsymbol{U}_{ex}$ is in equilibrium state and the numerical initial condition is defined as $\boldsymbol{U}=\mathcal{P}^k\boldsymbol{U}_{ex}$, we have $\boldsymbol{U}^e=\boldsymbol{U}$ and $\boldsymbol{U}^f=0$.

3.2.2 The source term approximation

Next, we will present the approximation of the source term $\int_K \boldsymbol{S}(\boldsymbol{U},\nabla\phi)\cdot\boldsymbol{\varphi}\mathrm{d}\boldsymbol{x}$. In [34], the source term approximation is designed as follows:

$$\int_K \boldsymbol{S}\left(\boldsymbol{U}^f,\nabla\phi_h\right)\cdot\boldsymbol{\varphi}\mathrm{d}\boldsymbol{x}-\int_K \boldsymbol{F}(\boldsymbol{U}^e):\nabla\boldsymbol{\varphi}\mathrm{d}\boldsymbol{x}+\int_{\partial K}\left(\boldsymbol{F}\left(\boldsymbol{U}^{e,int_K}\right)\cdot\boldsymbol{n}\right)\cdot\boldsymbol{\varphi}^{int_K}\mathrm{d}s, \tag{3.8}$$

where $\boldsymbol{S}(\boldsymbol{U},\nabla\phi_h)$ is decomposed into the sum of $\boldsymbol{S}\left(\boldsymbol{U}^f,\nabla\phi_h\right)$ and $\boldsymbol{S}(\boldsymbol{U}^e,\nabla\phi_h)$, and the approximation of the last term is converted into the flux, using equation satisfied by the equilibrium state. Here, ϕ_h is the projection of ϕ in space $\mathcal{V}^k$ (for example, the standard L^2 projection is often used). We have found out that, although the accuracy test carried out in [34] demonstrated the optimal convergence rate of the proposed well-balanced DG method with this choice of source term approximation, some additional numerical tests with manufactured solutions suggest that suboptimal convergence rate could be observed with this choice of source term approximation. Therefore, we propose an improvement of the source term approximation to ensure optimal convergence for all the numerical tests we tried.

Since ϕ_h is the projection of ϕ in space $\mathcal{V}^k$, taking its derivative in (3.8) might cause the lost of optimal convergence rate. Utilizing the fact that $\boldsymbol{U}_K^r$ is the reference equilibrium state, we have

$$\nabla\phi = -\nabla p_K^r/\rho_K^r, \tag{3.9}$$

following the definition of the equilibrium state (2.1). Therefore, we introduce a projection with one degree higher

$$\boldsymbol{U}^{\tilde{e}} = \mathcal{P}^{k+1}\boldsymbol{U}^r \tag{3.10}$$

to provide a high-order approximation of $\nabla\phi$, which is then defined as

$$\nabla\phi \approx -\nabla p_K^{\tilde{e}}/\rho_K^e, \tag{3.11}$$

where $p^{\tilde{e}}$ can be computed from $\boldsymbol{U}^{\tilde{e}}$. In addition, since $\boldsymbol{U}_K^r$ is in equilibrium state, we have

$$\int_K \boldsymbol{S}(\boldsymbol{U}^r,\nabla\phi)\cdot\boldsymbol{\varphi}\mathrm{d}\boldsymbol{x} = -\int_K \boldsymbol{F}(\boldsymbol{U}^r):\nabla\boldsymbol{\varphi}\mathrm{d}\boldsymbol{x} + \int_{\partial K}\left(\boldsymbol{F}\left(\boldsymbol{U}^{r,int_K}\right)\cdot\boldsymbol{n}\right)\cdot\boldsymbol{\varphi}^{int_K}\mathrm{d}\boldsymbol{s}, \tag{3.12}$$

which yields the following high order approximation

$$\int_K \boldsymbol{S}(\boldsymbol{U}^e,\nabla\phi)\cdot\boldsymbol{\varphi}\mathrm{d}\boldsymbol{x} \approx -\int_K \boldsymbol{F}(\boldsymbol{U}^e):\nabla\boldsymbol{\varphi}\mathrm{d}\boldsymbol{x} + \int_{\partial K}\left(\boldsymbol{F}\left(\boldsymbol{U}^{\tilde{e},int_K}\right)\cdot\boldsymbol{n}\right)\cdot\boldsymbol{\varphi}^{int_K}\mathrm{d}\boldsymbol{s}. \tag{3.13}$$

With all these information, we can present our source term approximation S_K as

$$S_K = \int_K \boldsymbol{S}\left(\boldsymbol{U}^f, -\frac{\nabla p^{\tilde{e}}}{\rho^e}\right)\cdot\boldsymbol{\varphi}\mathrm{d}\boldsymbol{x} - \int_K \boldsymbol{F}(\boldsymbol{U}^e):\nabla\boldsymbol{\varphi}\mathrm{d}\boldsymbol{x} + \int_{\partial K}\left(\boldsymbol{F}\left(\boldsymbol{U}^{\tilde{e},int_K}\right)\cdot\boldsymbol{n}\right)\cdot\boldsymbol{\varphi}^{int_K}\mathrm{d}\boldsymbol{s}. \tag{3.14}$$

Note that for the high-order accuracy, we change the approximation of the derivative of ϕ in the first term of (3.14). In addition, we modify the cell boundary integral by utilizing $\boldsymbol{U}^{\tilde{e}}$ instead of $\boldsymbol{U}^e$, for the purpose of simplifying the proof of the positivity-preserving property. We refer the proof of Proposition 4.1 in Appendix B for the details.

3.2.3 Modified boundary values

We modify the boundary values to be used in the evaluation of well-balanced numerical fluxes. The modified boundary values $\boldsymbol{U}^{b,int/ext_K} \in G$ are given by

$$\begin{aligned}
&\rho^{b,int_K} = \max\left(0,\rho^{*,int_K}\right), \qquad \rho^{b,ext_K} = \max\left(0,\rho^{*,ext_K}\right),\\
&\boldsymbol{m}^{b,int_K} = \rho^{b,int_K}\boldsymbol{u}^{int_K}, \qquad \boldsymbol{m}^{b,ext_K} = \rho^{b,ext_K}\boldsymbol{u}^{ext_K},\\
&E^{b,int_K} = \max\left(0,\mathcal{G}(\boldsymbol{U}^{*,int_K})\right) + \frac{1}{2}\rho^{b,int_K}\left\|\boldsymbol{u}^{int_K}\right\|^2,\\
&E^{b,ext_K} = \max\left(0,\mathcal{G}(\boldsymbol{U}^{*,ext_K})\right) + \frac{1}{2}\rho^{b,ext_K}\left\|\boldsymbol{u}^{ext_K}\right\|^2,
\end{aligned} \tag{3.15}$$

where the operator $\mathcal{G}$ is defined in Section 2.2, and $\boldsymbol{U}^{*,int_K}$, $\boldsymbol{U}^{*,ext_K}$ take the form

$$\boldsymbol{U}^{*,int_K} = \boldsymbol{U}^{\tilde{e},int_K} + \boldsymbol{U}^{f,int_K}, \quad \boldsymbol{U}^{*,ext_K} = \boldsymbol{U}^{\tilde{e},ext_K} + \boldsymbol{U}^{f,ext_K}. \tag{3.16}$$

Remark 3.2. One obvious difference between this approach and that in [34] lies in the choice of cell boundary values defined in (3.15). They play an important role in the proof of positivity-preserving property as outlined in the next section. In most cases, although the cell boundary values $\boldsymbol{U}^{int/ext_K} \in G$ for the positivity-preserving schemes, the well-balanced cell boundary values $\boldsymbol{U}^{*,int/ext}$ may not belong to G. These cell boundary values are chosen to be in the admissible state G and to keep the fluid velocity unchanged, which is crucial and greatly simplifies the proof process for the positivity-preserving property.

Another important change is the introduction of a higher-order polynomial $\boldsymbol{U}^{\tilde{e}}$ in the source term approximation, which can prevent the well-balanced scheme from yielding a sub-optimal convergence rate on some accuracy tests. We note that one can replace $\boldsymbol{U}^{\tilde{e}}$ with $\boldsymbol{U}^{e}$ in our well-balanced scheme and the obtained scheme still has the well-balanced and positivity-preserving properties.

3.2.4 The semi-discrete well-balanced scheme

The semi-discrete well-balanced DG scheme is defined as follows: for any test function $\boldsymbol{\varphi} \in \boldsymbol{\Pi}_d^k$, find $\boldsymbol{U} \in \boldsymbol{\Pi}_d^k$, such that

$$\frac{d}{dt}\int_K \boldsymbol{U}\cdot\boldsymbol{\varphi}\mathrm{d}\boldsymbol{x} = \boldsymbol{\mathcal{L}}_K(\boldsymbol{U}) \tag{3.17}$$

holds, with the right-hand side given by

$$\boldsymbol{\mathcal{L}}_K(\boldsymbol{U}) = \int_K \boldsymbol{F}(\boldsymbol{U}) : \nabla\boldsymbol{\varphi}\mathrm{d}\boldsymbol{x} - \int_{\partial K} \hat{\boldsymbol{F}}\left(\boldsymbol{U}^{b,int_K}, \boldsymbol{U}^{b,ext_K}, \boldsymbol{n}\right)\cdot\boldsymbol{\varphi}\mathrm{d}\boldsymbol{s} + S_K. \tag{3.18}$$

Here the source term approximation S_K is defined in (3.14). The numerical flux $\hat{\boldsymbol{F}}$ is a monotone numerical flux of $\boldsymbol{F}(\boldsymbol{U})$ with $\boldsymbol{U}^{b,int_K}$ and $\boldsymbol{U}^{b,ext_K}$ defined in (3.15). In this paper, the simple LF flux defined in (2.12) is used.

The fully discrete Runge-Kutta discontinuous Galerkin (RKDG) method can be obtained by coupling the semi-discrete method with high-order strong stability preserving (SSP) Runge-Kutta time discretizations [20]. The following third order SSP Runge-Kutta methods:

$$\begin{aligned}
&\int_K \boldsymbol{U}^{(1)}\cdot\boldsymbol{\varphi}\mathrm{d}\boldsymbol{x} = \int_K \boldsymbol{U}^{n}\cdot\boldsymbol{\varphi}\mathrm{d}\boldsymbol{x} + \Delta t\boldsymbol{\mathcal{L}}_K(\boldsymbol{U}^n),\\
&\int_K \boldsymbol{U}^{(2)}\cdot\boldsymbol{\varphi}\mathrm{d}\boldsymbol{x} = \frac{3}{4}\int_K \boldsymbol{U}^{n}\cdot\boldsymbol{\varphi}\mathrm{d}\boldsymbol{x} + \frac{1}{4}\left(\int_K \boldsymbol{U}^{(1)}\cdot\boldsymbol{\varphi}\mathrm{d}\boldsymbol{x} + \Delta t\boldsymbol{\mathcal{L}}_K\left(\boldsymbol{U}^{(1)}\right)\right),\\
&\int_K \boldsymbol{U}^{n+1}\cdot\boldsymbol{\varphi}\mathrm{d}\boldsymbol{x} = \frac{1}{3}\int_K \boldsymbol{U}^{n}\cdot\boldsymbol{\varphi}\mathrm{d}\boldsymbol{x} + \frac{2}{3}\left(\int_K \boldsymbol{U}^{(2)}\cdot\boldsymbol{\varphi}\mathrm{d}\boldsymbol{x} + \Delta t\boldsymbol{\mathcal{L}}_K\left(\boldsymbol{U}^{(2)}\right)\right),
\end{aligned} \tag{3.19}$$

is used in this paper, where $\boldsymbol{\mathcal{L}}_K(\boldsymbol{U})$ is defined in (3.17).

Remark 3.3. One can observe that the proposed scheme (3.17) has a simpler numerical flux, when compared with the well-balanced methods in [34]. We choose the special

projection $\mathcal{P}^k$ which is continuous at the cell boundaries if the numerical solution equals the equilibrium states. This helps us to simplify the well-balanced numerical flux and the proof of the positivity-preserving property in the next section. Similar numerical flux has been introduced in [10] based on nodal DG methods.

3.3 Well-balanced property

Following the steps in Section 3.2.4, we establish a well-balanced RKDG method for the Euler equations with gravitation. We first summarize all the variables in our scheme before proving the well-balanced property:

- $\boldsymbol{U}_K^r \notin \mathbb{P}^k(K)$, the recovery equilibrium, is defined for each cell K in Section 3.1;
- $\boldsymbol{U}_K^e = \mathcal{P}^k \boldsymbol{U}_K^r \in \mathbb{P}^k(K)$, is the equilibrium part of $\boldsymbol{U}_K$ in (3.7);
- $\boldsymbol{U}_K^f = \boldsymbol{U}_K - \boldsymbol{U}_K^e \in \mathbb{P}^k(K)$ is the fluctuation part of $\boldsymbol{U}_K$ in (3.7);
- $\boldsymbol{U}_K^{\tilde{e}} = \mathcal{P}^{k+1} \boldsymbol{U}_K^r \in \mathbb{P}^{k+1}(K)$ is the projection of $\boldsymbol{U}_K^r$ into a polynomial with degree $k+1$, defined in (3.10). It is introduced for the optimal source term approximation;
- $\boldsymbol{U}_K^b$ in (3.15) is defined on ∂K, and is used in the numerical flux.

Proposition 3.1. The RKDG scheme for the Euler equations with gravity described in (3.17) coupled with (3.19) maintains the polytropic and the isothermal equilibrium state exactly in discrete level.

Proof. Suppose that the initial condition $\boldsymbol{U}_{ex}(\boldsymbol{x},0)$ is the polytropic or the isothermal equilibrium state, or any other known zero-velocity equilibrium state. In order to prove our methods can maintain the equilibrium state in discrete level, it is sufficient to show that $\boldsymbol{\mathcal{L}}_K(\boldsymbol{U}) = 0$.

By the definition of $\boldsymbol{U}^r$ in Section 3.1, we note that $\boldsymbol{U}^r = \boldsymbol{U}_{ex}$ under the assumption that $\boldsymbol{U}_{ex}$ are the equilibrium state. Therefore, we have $\boldsymbol{U}^e = \boldsymbol{U}$ and $\boldsymbol{U}^f = 0$ following the definitions in (3.7). Moreover,

$$\boldsymbol{U}^{b,int_K} = \boldsymbol{U}^{b,ext_K} = \boldsymbol{U}^{\tilde{e},int_K}, \tag{3.20}$$

and the well-balanced numerical fluxes satisfy

$$\hat{\boldsymbol{F}}\left(\boldsymbol{U}^{b,int_K}, \boldsymbol{U}^{b,ext_K}, \boldsymbol{n}\right) = \hat{\boldsymbol{F}}\left(\boldsymbol{U}^{b,int_K}, \boldsymbol{U}^{b,int_K}, \boldsymbol{n}\right) = \boldsymbol{F}\left(\boldsymbol{U}^{\tilde{e},int_K}\right) \cdot \boldsymbol{n}, \tag{3.21}$$

where the first equality is due to (3.20) and the second equality use the consistent property of the numerical flux

$$\hat{\boldsymbol{F}}(\boldsymbol{V}, \boldsymbol{V}, \boldsymbol{n}) = \boldsymbol{F}(\boldsymbol{V}) \cdot \boldsymbol{n}.$$

Therefore we have

$$\begin{aligned}\mathcal{L}_K(\boldsymbol{U}) &= \int_K \boldsymbol{F}(\boldsymbol{U}) : \nabla\boldsymbol{\varphi}\mathrm{d}\boldsymbol{x} - \int_{\partial K}\left(\boldsymbol{F}\left(\boldsymbol{U}^{\tilde{e},int_K}\right)\cdot\boldsymbol{n}\right)\cdot\boldsymbol{\varphi}^{int_K}\mathrm{d}\boldsymbol{s} + S_K \\ &= \int_K \boldsymbol{F}(\boldsymbol{U}) : \nabla\boldsymbol{\varphi}\mathrm{d}\boldsymbol{x} - \int_{\partial K}\left(\boldsymbol{F}\left(\boldsymbol{U}^{\tilde{e},int_K}\right)\cdot\boldsymbol{n}\right)\cdot\boldsymbol{\varphi}^{int_K}\mathrm{d}\boldsymbol{s} \\ &\quad - \int_K \boldsymbol{F}(\boldsymbol{U}) : \nabla\boldsymbol{\varphi}\mathrm{d}\boldsymbol{x} + \int_{\partial K}\left(\boldsymbol{F}\left(\boldsymbol{U}^{\tilde{e},int_K}\right)\cdot\boldsymbol{n}\right)\cdot\boldsymbol{\varphi}^{int_K}\mathrm{d}\boldsymbol{s} \\ &= 0,\end{aligned}$$

where the first equality is due to the definition of $\mathcal{L}_K(\boldsymbol{U})$ and (3.21), the second equality is due to (3.14) and $\boldsymbol{U}^f = 0$ and $\boldsymbol{U}^e = \boldsymbol{U}$. We conclude that $\mathcal{L}_K(\boldsymbol{U}) = 0$ when the initial condition $\boldsymbol{U}_{ex}$ is the equilibrium state. When we apply the time discretization (3.19), the numerical solution won't change over time, which means that our method maintains the equilibrium state exactly in the discrete level. □

4 Positivity-preserving well-balanced DG methods

In this section, we show that the well-balanced DG scheme (3.17) has a weak positivity property under a suitable condition for the time step. With such weak positivity, a simple scaling limiter can enforce the positivity-preserving property without losing conservation and high-order accuracy.

4.1 Properties of admissible states

We start by introducing some properties of the admissible states (2.7), which will be used to prove the weak positive property. The first two properties are taken from [49].

Lemma 4.1 ([49]). *The set of admissible states G defined in* (2.7) *is a convex set.*

Lemma 4.2 ([49]). *For any $\boldsymbol{U} \in G$ and $\|\boldsymbol{n}\| = 1$, we have*

$$\boldsymbol{U} - \eta\boldsymbol{F}(\boldsymbol{U})\cdot\boldsymbol{n} \in G, \tag{4.1}$$

if $\eta \in \mathbb{R}$ satisfies

$$\alpha_0|\eta| \le 1, \tag{4.2}$$

where

$$\alpha_0 = |\boldsymbol{u}\cdot\boldsymbol{n}| + \frac{p}{\rho\sqrt{2e}}. \tag{4.3}$$

The next two lemmas are introduced to analyze the impact of the well-balanced numerical fluxes in the proof of weak positivity property.

Lemma 4.3. *For any $\boldsymbol{U}$, $\boldsymbol{U}^*\in G$ with the same velocity $\boldsymbol{u}=\boldsymbol{u}^*$, we have*

$$\boldsymbol{U}-\eta\boldsymbol{U}^*\in G, \tag{4.4}$$

if the positive constant $\eta>0$ satisfies

$$\alpha_0\eta<1, \tag{4.5}$$

where

$$\alpha_0=\max\left(\frac{\rho^*}{\rho},\frac{p^*}{p}\right).$$

Proof. It is straight forward to observe that the first component of $\boldsymbol{U}-\eta\boldsymbol{U}^*$ is positive:

$$\rho-\eta\rho^*>\rho-\frac{\rho^*}{\alpha_0}\geq\rho-\frac{\rho}{\rho^*}\rho^*=0.$$

Therefore, we only need to show the pressure is also positive, which follows from the following steps:

$$\begin{aligned}\mathcal{G}(\boldsymbol{U}-\eta\boldsymbol{U}^*)&=E-\eta E^*-\frac{1}{2}\frac{\|\boldsymbol{m}-\eta\boldsymbol{m}^*\|^2}{\rho-\eta\rho^*}=E-\eta E^*-\frac{1}{2}(\rho-\eta\rho^*)\|\boldsymbol{u}\|^2\\&=\rho e+\frac{1}{2}\rho\|\boldsymbol{u}\|^2-\eta\left((\rho e)^*+\frac{1}{2}\rho^*\|\boldsymbol{u}\|^2\right)-\frac{1}{2}(\rho-\eta\rho^*)\|\boldsymbol{u}\|^2\\&=\frac{p}{\gamma-1}-\eta\frac{p^*}{\gamma-1}=\left(1-\eta\frac{p^*}{p}\right)\rho e>\left(1-\frac{1}{\alpha_0}\frac{p^*}{p}\right)\rho e\geq 0,\end{aligned}$$

where the second and third equalities utilize the fact that $\boldsymbol{u}=\boldsymbol{u}^*$, the fourth and fifth equalities follow from the definition of $p=(\gamma-1)\rho e$, and the last two inequalities holds under the condition (4.5). This finishes the proof. □

Lemma 4.4. *For any $\boldsymbol{U}$, $\boldsymbol{U}^*\in G$ with the same velocity $\boldsymbol{u}=\boldsymbol{u}^*$ and $\|\boldsymbol{n}\|=1$, we have*

$$\boldsymbol{U}-\eta\boldsymbol{F}(\boldsymbol{U}^*)\cdot\boldsymbol{n}\in G, \tag{4.6}$$

if $\eta>0$ satisfies

$$\alpha_0\alpha_1\eta<1, \tag{4.7}$$

where

$$\alpha_0=\max\left(\frac{p^*}{p},\frac{\rho^*}{\rho}\right),\quad \alpha_1=|\boldsymbol{u}\cdot\boldsymbol{n}|+\frac{p}{\rho\sqrt{2e}}.$$

The proof of this lemma is shown in Appendix A.

4.2 Positivity of the high order DG methods

In this subsection, we will prove a weak positivity property of the proposed well-balanced DG scheme.

We begin with presenting the quadrature rule used to approximate the integrals. Let us denote a set of 2D quadrature nodes with positive weights on the cell K by $\{\hat{\boldsymbol{x}}_K^\mu, \hat{\omega}_K^\mu\}_{1\le\mu\le L'}$ and introduce the following quadrature rule

$$\int_K g(\boldsymbol{U})\,\mathrm{d}\boldsymbol{x} = \sum_{\mu=1}^{L} \hat{\omega}_K^\mu\, g\Big(\boldsymbol{U}_K\big(\hat{\boldsymbol{x}}_K^\mu\big)\Big). \tag{4.8}$$

On the edge F_K^ν of the cell K, we introduce a set of 1D quadrature nodes with positive weights by $\{\tilde{\boldsymbol{x}}_{F_K^\nu}^\mu, \tilde{\omega}_K^\mu\}_{1\le\mu\le N}$, and the following quadrature rule

$$\int_{F_K^\nu} g(\boldsymbol{U})\,\mathrm{d}\boldsymbol{s} = \sum_{\mu=1}^{N} \tilde{\omega}_{F_K^\nu}^\mu g\Big(\boldsymbol{U}^{int_K}\Big(\tilde{\boldsymbol{x}}_{F_K^\nu}^\mu\Big)\Big). \tag{4.9}$$

In our computation, the Gaussian quadrature rule is used for both 1D edge and 2D volume integrals. We choose enough quadrature points such that the quadrature rule is exact for integrals of polynomials up to k on the cell K and $k+1$ on the face F_K^ν.

Further, another special quadrature rule is needed (only) in the proof of weak positivity property. Such special d dimension quadrature on the cell K should satisfy:

- The quadrature rule has positive weights and is exact for integrals of polynomials of degree up to k on the cell K;
- The set of the quadrature points must include all the quadrature points $\tilde{\boldsymbol{x}}_{F_K^\nu}^\mu$, $\mu = 1,\cdots,N$ on the edges $F_K^\nu \in \partial K$, $\nu = 1,\cdots,d+1$.

In one dimension, we note that the Gauss-Lobatto quadrature rule is an eligible choice. For two-dimensional case on triangular meshes, some examples of these quadrature rules are presented in [50]. This quadrature rule ensures that the cell average of the computational variable can be written as follows,

$$\bar{\boldsymbol{U}}_K = \sum_{\nu=1}^{d+1}\sum_{\mu=1}^{N} \tilde{\omega}_{F_K^\nu}^\mu \boldsymbol{U}^{int_K}\Big(\tilde{\boldsymbol{x}}_{F_K^\nu}^\mu\Big) + \sum_{\mu=1}^{\tilde{L}} \tilde{\omega}_K^\mu \boldsymbol{U}_K\big(\tilde{\boldsymbol{x}}_K^\mu\big), \tag{4.10}$$

where $\{\tilde{\boldsymbol{x}}_{F_K^\nu}^\mu\}$ are quadrature points on the boundary of K and $\{\tilde{\boldsymbol{x}}_K^\mu\}$ are quadrature points inside K, and $\{\tilde{\omega}_{F_K^\nu}^\mu\}$ and $\{\tilde{\omega}_K^\mu\}$ are the corresponding quadrature weights.

We define the following set

$$\mathbb{S}_K = \Big\{\tilde{\boldsymbol{x}}_{F_K^\nu}^\mu,\ \mu=1,\cdots,N,\ \nu=1,\cdots,d+1\Big\} \bigcup \{\tilde{\boldsymbol{x}}_K^\mu,\ \mu=1,\cdots,\tilde{L}\} \bigcup \{\hat{\boldsymbol{x}}_K^\mu,\ \mu=1,\cdots,L\},$$

that includes all the quadrature points discussed above, and the set of all the quadrature points on the boundary of K

$$\mathbb{Q}_K=\left\{\tilde{\boldsymbol{x}}_{F_K^\nu}^\mu,\ \mu=1,\cdots,N,\ \nu=1,\cdots,d+1\right\}. \tag{4.11}$$

Again, we would like to emphasize that the quadrature rule (4.10) is introduced to be used in the proof, and only the quadrature rule (4.8) for the volume integral on K and the quadrature rule (4.9) for the line integral over ∂K are applied in the implementation of our proposed scheme.

Next, we are ready to present the weak positivity property of our scheme.

Proposition 4.1. Consider the well-balanced numerical methods in (3.18)-(3.19). If $\boldsymbol{U}_K^n(\boldsymbol{x})\in G$ holds for any $\boldsymbol{x}\in\mathbb{S}_K$, we have

$$\bar{\boldsymbol{U}}_K^{n+1}\in G, \tag{4.12}$$

under the CFL-type condition

$$\hat{\alpha}_0\Delta t<1, \tag{4.13}$$

with

$$\begin{aligned}
&\hat{\alpha}_0=\hat{\alpha}_F+\hat{\alpha}_S,\\
&\hat{\alpha}_F=\hat{\alpha}_1\alpha\max_{\nu,\mu}\frac{\tilde{\omega}_{F_K^\nu}^\mu|F_K^\nu|}{\tilde{\omega}_{F_K^\nu}^\mu\Delta_K},\qquad \hat{\alpha}_1=\max_{\boldsymbol{x}\in\mathbb{Q}_K}\left(\frac{\rho_K^b(\boldsymbol{x})}{\rho_K^n(\boldsymbol{x})},\frac{p_K^b(\boldsymbol{x})}{p_K^n(\boldsymbol{x})}\right),\\
&\hat{\alpha}_S=\max_{\boldsymbol{x}\in\mathbb{S}_K}\frac{\left\|\nabla p_K^{\tilde{e}}(\boldsymbol{x})/\rho_K^e(\boldsymbol{x})\right\|}{\sqrt{2e_K^n(\boldsymbol{x})}},
\end{aligned}$$

and α being the parameter of LF flux defined in (2.13).

The proof of this proposition is shown in Appendix B.

Remark 4.1. We note that the term

$$\max_{\nu,\mu}\frac{\tilde{\omega}_{F_K^\nu}^\mu|F_K^\nu|}{\tilde{\omega}_{F_K^\nu}^\mu\Delta_K}$$

in the definition of $\hat{\alpha}_F$ depends on the chosen quadrature rule. A few examples are provided below to demonstrate its value.

- In the one-dimensional case, if the Gauss-Lobatto quadrature rule is used, we have

$$\tilde{\omega}_{F_K^\nu}^\mu=\frac{1}{6},\ \text{ for } k=2,3,\qquad \tilde{\omega}_{F_K^\nu}^\mu=\frac{1}{12},\ \text{ for } k=4,5,$$

and $\tilde{\omega}^{\mu}_{F^{\nu}_K}=1$ and $|F^{\nu}_K|=1$. Therefore,

$$\hat{\alpha}_F=6\hat{\alpha}_1\alpha/\Delta_K, \quad \text{for } k=2,3$$

and

$$\hat{\alpha}_F=12\hat{\alpha}_1\alpha/\Delta_K, \quad \text{for } k=4,5.$$

- In the two-dimensional case, we can use the quadrature rule shown in [50, Figure 3.2]. For $k=2$, we have

$$\max_{\nu,\mu}\frac{\tilde{\omega}^{\mu}_{F^{\nu}_K}}{\tilde{\omega}^{\mu}_{F^{\nu}_K}}=9,$$

which means that

$$\hat{\alpha}_F=\frac{9\hat{\alpha}_1\alpha\max_{\nu}|F^{\nu}_K|}{\Delta_K}.$$

For example with a 30-60-90 triangle, we have

$$\max_{\nu}\frac{|F^{\nu}_K|}{\Delta_K}=2\sqrt{\frac{\frac{2}{\sqrt{3}}}{\Delta_K}}, \quad \hat{\alpha}_F\approx\frac{19.3\hat{\alpha}_1\alpha}{\sqrt{\Delta_K}}.$$

Remark 4.2. In the one-dimensional case, one can show that $\hat{\alpha}_1\equiv 1$, which simplifies the definition of $\hat{\alpha}_0$. This follows from the fact that both $\boldsymbol{U}^{\tilde{e}}$ and $\boldsymbol{U}^{e}$ share the same value with $\boldsymbol{U}^{r}$ at the cell boundaries, which consist of the end points of the interval and equal to the point set $\mathbb{Q}_K$ in the 1D setting. Therefore, one can conclude that $\boldsymbol{U}^{*,int_K}(\boldsymbol{x})=\boldsymbol{U}^{int_K}(\boldsymbol{x})$ for any $\boldsymbol{x}\in\mathbb{Q}_K$, and also $\boldsymbol{U}^{b,int_K}(\boldsymbol{x})=\boldsymbol{U}^{int_K}(\boldsymbol{x})$ due to the assumption of Proposition 4.1 that $\boldsymbol{U}^{int_K}(\boldsymbol{x})\in G$. Similarly, $\boldsymbol{U}^{b,ext_K}(\boldsymbol{x})=\boldsymbol{U}^{ext_K}(\boldsymbol{x})$ can be obtained, which leads to the conclusion that $\hat{\alpha}_1\equiv 1$.

In the two-dimensional case, the value of $\hat{\alpha}_1$ is more complicated, as the sets of quadrature points and projection points may not be the same. But we can show that $\hat{\alpha}_1=1+\mathcal{O}(h^{k+1})$ with k being the polynomial degree, namely, it will decrease to 1 as mesh is refined. In the numerical examples, we also track and report the value of $\hat{\alpha}_1$, which confirms this result.

4.3 Positivity-preserving limiter

If the weak positivity property holds, i.e. $\bar{\boldsymbol{U}}_K\in G$ at the time step t^{n+1}, a simple positivity-preserving limiter [50] can be applied to enforce that $\boldsymbol{U}_K(\boldsymbol{x})\in G$, $\forall\boldsymbol{x}\in\mathbb{S}_K$. We define the positivity-preserving limiting operator Θ as

$$\Theta\boldsymbol{U}_K=\theta^{(2)}_K\left(\hat{\boldsymbol{U}}_K(\boldsymbol{x})-\bar{\boldsymbol{U}}_K\right)+\bar{\boldsymbol{U}}_K, \tag{4.14}$$

with

$$\theta_K^{(2)} = \min\left(1, \frac{\mathcal{G}(\bar{\boldsymbol{U}}_K) - \epsilon}{\mathcal{G}(\bar{\boldsymbol{U}}_K) - \min_{\boldsymbol{x}\in S_K} \mathcal{G}(\hat{\boldsymbol{U}}_K(\boldsymbol{x}))}\right), \tag{4.15}$$

$$\hat{\boldsymbol{U}}_K(\boldsymbol{x}) = (\hat{\rho}_K(\boldsymbol{x}), \boldsymbol{m}_K(\boldsymbol{x}), E_K(\boldsymbol{x}))^T, \tag{4.16}$$

$$\hat{\rho}_K = \theta_K^{(1)}(\rho_K - \bar{\rho}_K) + \bar{\rho}_K, \tag{4.17}$$

$$\theta_K^{(1)} = \min\left(1, \frac{\bar{\rho}_K - \epsilon}{\bar{\rho}_K - \min_{\boldsymbol{x}\in S_K} \rho_K(\boldsymbol{x})}\right). \tag{4.18}$$

Here ϵ is a sufficiently small positive number, introduced to avoid the effect of the round-error. For example, we can take $\epsilon = \min\left(10^{-13}, \bar{\rho}_K, \mathcal{G}(\bar{\boldsymbol{U}}_K)\right)$. The limiter Θ doesn't destroy the high-order accuracy and keeps the mass conservation. We refer to [50] for the details and the proof.

We apply the limiter Θ to $\boldsymbol{U}_K$ at each Runge-Kutta stage in our methods. Based on Proposition 4.1, the resulting DG methods have the positivity-preserving property under suitable time step conditions.

4.4 Algorithm

Finally, we summarize the steps of our high-order positivity-preserving well-balanced DG scheme as follows:

1. For any given initial condition $\boldsymbol{U}_{ex}(\boldsymbol{x},0)$, we project it into the piecewise polynomial space $\boldsymbol{\Pi}_d^k$ to obtain the numerical initial condition:

$$\boldsymbol{U}^0 = \mathcal{P}^k(\boldsymbol{U}_{ex}(\boldsymbol{x},0)); \tag{4.19}$$

2. At each Runge-Kutta stage, a reference equilibrium state $\boldsymbol{U}^r$ is computed following the idea in Section 3.1. We then decompose the numerical solution $\boldsymbol{U}$ into two parts: the equilibrium part $\boldsymbol{U}^e$ and the fluctuation part $\boldsymbol{U}^f$. We also compute $\boldsymbol{U}^{\tilde{e}}$ following the definition in Eq. (3.10);

3. Update $\boldsymbol{U}$ by applying the positivity-preserving limiter Θ defined in (4.14):

$$\widetilde{\boldsymbol{U}} = \Theta\boldsymbol{U}. \tag{4.20}$$

   We still denote them by $\boldsymbol{U}$ for simplicity;

4. Evaluate the modified cell boundary values (3.15) and apply the LF numerical flux (2.12). We note that for the steady state solutions, the modified cell boundary values $\boldsymbol{U}^{b,int_K} = \boldsymbol{U}^{b,int_K}$ and the dissipation term in LF flux turns out to be zero due to the consistency of LF flux;

5. Compute the source term approximation in (3.14);

6. Evaluate the spatial operator $\boldsymbol{\mathcal{L}}_K(\boldsymbol{U})$ in (3.17), and apply the SSP Runge-Kutta method (3.19) to advance in time. For each Runge-Kutta stage, we repeat the steps 2-5.

5 Numerical examples

In this section, we provide some one- and two-dimensional numerical results to demonstrate the numerical performance of the proposed scheme. In most of our examples, we use $\mathbb{P}^2$ piecewise polynomials unless otherwise stated. In most of the two-dimensional examples, the uniform criss-triangles are used. In all the examples, the time step size is set as

$$\Delta t = 0.8/\hat{\alpha}_0, \tag{5.1}$$

where $\hat{\alpha}_0$ satisfies the time step constraints (4.13) in all cells K for one-dimensional and two-dimensional cases.

5.1 Numerical examples in one dimension

Example 5.1. Test for the accuracy in one dimension.

In this example, we test the orders of accuracy of the proposed methods in the one-dimensional setting. We follow the setup in [33] and consider the simple steady-state exact solution given by

$$\begin{aligned}
&\rho(x,t) = \exp(-x),\\
&u(x,t) = 0,\\
&p(x,t) = (1+x)\exp(-x),
\end{aligned}$$

on a unit domain $[0,1]$ with gravitational field $\phi(x) = \frac{1}{2}x^2$. The exact solutions are applied at the ghost cells near the boundaries. We set the stop time $T = 0.1$. We choose the isothermal equilibrium recovery in this example. The L^1 errors and orders for cases $k = 1,2,3$ are shown in Table 1, from which we can see that our scheme have the desired high order accuracy.

Example 5.2. Additional 1D accuracy test for comparison with the scheme in [34].

Optimal convergence rate of the proposed positivity-preserving well-balanced DG method was observed in the previous example, for which the method in [34] also demonstrated optimal convergence. In this example, we will provide another accuracy test, and show that these two methods demonstrate different convergence rates for this example. We consider a manufactured exact solution of the form

$$\begin{aligned}
&\rho(x,t) = \exp(x-t),\\
&u(x,t) = 1,\\
&p(x,t) = 1,
\end{aligned}$$

Table 1: Example 5.1, L^1 errors and orders of accuracy with the case $k=1,2,3$.

$k=1$	ρ		ρu		E	
N	L^1 error	order	L^1 error	order	L^1 error	order
40	2.60E-05	-	6.69E-06	-	4.69E-05	-
80	6.51E-06	2.00	1.67E-06	2.00	1.17E-05	2.00
160	1.63E-06	2.00	4.16E-07	2.00	2.94E-06	2.00
320	4.07E-07	2.00	1.04E-07	2.00	7.34E-07	2.00
$k=2$	ρ		ρu		E	
N	L^1 error	order	L^1 error	order	L^1 error	order
10	5.07E-06	-	2.13E-06	-	8.57E-06	-
20	6.35E-07	3.00	2.60E-07	3.04	1.08E-06	2.99
40	7.93E-08	3.00	3.22E-08	3.01	1.35E-07	3.00
80	9.91E-09	3.00	4.01E-09	3.01	1.69E-08	3.00
$k=3$	ρ		ρu		E	
N	L^1 error	order	L^1 error	order	L^1 error	order
10	5.41E-08	-	5.05E-08	-	1.43E-07	-
20	3.08E-09	4.13	2.65E-09	4.25	7.60E-09	4.24
40	1.91E-10	4.01	1.76E-10	3.91	4.78E-10	3.99
80	1.19E-11	4.00	1.09E-11	4.01	2.97E-11	4.01

which satisfies the modified Euler equation given by

$$\boldsymbol{U}_t+\partial_x \boldsymbol{F}(\boldsymbol{U})=\boldsymbol{S}(\boldsymbol{U},\phi_x)+\boldsymbol{\Phi}, \tag{5.2}$$

with

$$\phi(x)=\exp(x), \quad \boldsymbol{\Phi}=(0,\exp(2x-t),\exp(2x-t))^T.$$

The computational domain is set as $[0,1]$. The exact solutions are applied at the ghost cells near the boundaries. We set the stop time $T=1$. We choose the isothermal equilibrium recovery in this example. The L^1 errors and orders for cases $k=1,2,3$ of our proposed DG methods are shown in Table 2, from which we observe the desired high order accuracy for all choices of k. The results of the DG methods in [34] are shown in Table 3, and suboptimal convergence rates are observed for $k=1$ (the variables ρ, ρu and E), $k=2$ (the variables ρ, ρu and E) and $k=3$ (the variables ρ, ρu and E). This justifies the high order modification of the source term approximation, described in the Section 3.2.

Example 5.3. Accuracy test for low density.

In this example, we test the orders of accuracy when the solution involves low density and the positivity-preserving limiter takes effect in one dimension. We consider another

Table 2: Example 5.2, L^1 errors and orders of accuracy with the case $k=1,2,3$.

$k=1$	ρ		ρu		E	
N	L^1 error	order	L^1 error	order	L^1 error	order
40	1.08E-03	-	3.07E-04	-	3.46E-03	-
80	2.64E-04	2.04	7.73E-05	1.99	8.25E-04	2.07
160	6.12E-05	2.11	1.88E-05	2.04	1.92E-04	2.10
320	1.47E-05	2.06	4.62E-06	2.03	4.61E-05	2.06
$k=2$	ρ		ρu		E	
N	L^1 error	order	L^1 error	order	L^1 error	order
10	9.14E-04	-	2.61E-04	-	3.00E-03	-
20	1.05E-04	3.12	2.65E-05	3.30	3.27E-04	3.20
40	1.20E-05	3.14	2.67E-06	3.31	3.51E-05	3.22
80	1.43E-06	3.07	3.12E-07	3.10	4.10E-06	3.10
$k=3$	ρ		ρu		E	
N	L^1 error	order	L^1 error	order	L^1 error	order
10	1.66E-05	-	4.94E-06	-	5.60E-05	-
20	6.82E-07	4.60	1.94E-07	4.67	2.29E-06	4.61
40	3.59E-08	4.25	1.03E-08	4.25	1.21E-07	4.24
80	1.91E-09	4.23	5.72E-10	4.16	6.63E-09	4.19

Table 3: Example 5.2, L^1 errors and orders of accuracy with the case $k=1,2,3$, of the DG method in [34].

$k=1$	ρ		ρu		E	
N	L^1 error	order	L^1 error	order	L^1 error	order
40	6.95E-03	-	2.55E-03	-	2.29E-02	-
80	3.59E-03	0.95	1.32E-03	0.95	1.18E-02	0.96
160	1.77E-03	1.02	6.57E-04	1.00	5.83E-03	1.01
320	8.68E-04	1.03	3.26E-04	1.01	2.87E-03	1.02
$k=2$	ρ		ρu		E	
N	L^1 error	order	L^1 error	order	L^1 error	order
10	6.03E-04	-	2.42E-04	-	2.04E-03	-
20	1.41E-04	2.10	5.85E-05	2.05	4.63E-04	2.14
40	3.37E-05	2.07	1.41E-05	2.05	1.11E-04	2.06
80	7.87E-06	2.10	3.39E-06	2.06	2.61E-05	2.09
$k=3$	ρ		ρu		E	
N	L^1 error	order	L^1 error	order	L^1 error	order
10	1.64E-05	-	4.61E-06	-	5.42E-05	-
20	1.28E-06	3.68	3.93E-07	3.56	4.14E-06	3.71
40	1.39E-07	3.21	4.08E-08	3.26	4.34E-07	3.25
80	1.64E-08	3.08	4.90E-09	3.06	5.16E-08	3.07

Table 4: Example 5.3, L^1 errors and orders of accuracy with the case $k=1,2,3$.

$k=1$	ρ		ρu		E	
N	L^1 error	order	L^1 error	order	L^1 error	order
20	2.13E-01	-	3.41E-01	-	3.99E-01	-
40	4.23E-02	2.33	6.95E-02	2.29	7.76E-02	2.36
80	9.60E-03	2.14	1.63E-02	2.09	1.83E-02	2.09
160	2.30E-03	2.06	3.96E-03	2.04	4.45E-03	2.04
$k=2$	ρ		ρu		E	
N	L^1 error	order	L^1 error	order	L^1 error	order
10	6.44E-02	-	1.47E-02	-	1.74E-01	-
20	6.69E-03	3.27	1.58E-03	3.22	2.12E-02	3.03
40	5.38E-04	3.64	1.36E-04	3.54	1.66E-03	3.68
80	7.12E-05	2.92	9.54E-06	3.83	1.55E-04	3.41
$k=3$	ρ		ρu		E	
N	L^1 error	order	L^1 error	order	L^1 error	order
10	1.59E-02	-	9.94E-03	-	4.10E-02	-
20	8.41E-04	4.24	2.75E-04	5.17	2.01E-03	4.35
40	5.28E-05	3.99	1.42E-05	4.28	1.18E-04	4.09
80	3.13E-06	4.08	8.09E-07	4.13	7.38E-06	3.99

exact solution of equation (5.2):

$$\begin{aligned}&\rho(x,t)=1+0.99\sin(x-t),\\&u(x,t)=1,\\&p(x,t)=1,\end{aligned}$$

with $\gamma=1.4$,

$$\phi(x)=x,\quad \mathbf{\Phi}=(0,1+0.99\sin(x-t),1+0.99\sin(x-t))^T.$$

The computation domain is set as $[0,2\pi]$ and periodic boundary condition is applied. The minimum density for this test is 0.01. Without the positivity-preserving limiter, the standard DG scheme has trouble in long time simulation. We can use this example to test the accuracy when the positivity-preserving limiter takes effect. In this test, we set the stop time $t=4$ and choose the isothermal equilibrium recovery in this example. In Table 4, the L^1 errors and orders for $k=1,2,3$ of our proposed DG methods are shown. We observe the optimal convergence rate for all variables and polynomial degree k, which means that the positivity-preserving limiter does not affect the high-order accuracy.

Example 5.4. Test for the well-balanced property of the 1D polytropic equilibrium.

Table 5: Example 5.4, L^1 errors for the polytropic equilibrium with different precisions.

N	precision	ρ	ρu	E
100	double	9.31E-15	3.41E-15	9.97E-15
	quadruple	9.51E-33	2.67E-33	8.57E-33
200	double	1.40E-14	5.13E-15	1.53E-14
	quadruple	1.53E-32	4.38E-33	1.62E-32

This example is used to verify that the proposed DG scheme can maintain the polytropic equilibrium exactly for the 1D Euler equations and its ability to capture small perturbation of such equilibrium. We consider the following equilibrium state

$$\begin{aligned} &\rho(x) = (1-0.4x)^{1.5}, \\ &u(x) = 0, \\ &p(x) = (1-0.4x)^{2.5}, \end{aligned} \tag{5.3}$$

on a computational domain $[0,2]$ with the linear gravitational field $\phi(x) = x$ and $\gamma = 5/3$. We set the stop time $T = 2$ and the L^1 errors of the numerical solutions with different precisions are shown in Table 5. It can be observed that our scheme maintains the polytropic equilibrium state at a discrete level, and this confirms its well-balanced property.

Next, we impose a perturbation to the polytropic equilibrium (5.3) and test the capability of our scheme in capturing the propagation of this small perturbation. At the left boundary $x = 0$, we add a periodic velocity perturbation of the form

$$u(0,t) = A\sin(4\pi t),$$

with a small perturbation $A = 10^{-6}$. The stop time is set as $T = 1.5$, and 100 uniform cells are used. The numerical solutions are shown in Fig. 3. For comparison, we include the reference solutions computed on the refined mesh with $N = 2000$, and also show the results of the third order traditional non-well-balanced (non-WB) DG method in the same figure. We can observe that the well-balanced DG method produces numerical results consistent with the reference solutions, while the solutions of the non-WB method does not agree well with the reference solution, especially in the region near the right boundary. In addition, we record the CPU time of our proposed scheme and standard DG scheme for this test. The CPU time of standard DG scheme is 3.78s and that of our proposed scheme is 4.94s. We find that although our proposed scheme carries some overhead and is slower than standard methods, the numerical solution of our proposed scheme performs much better than standard DG scheme.

Example 5.5. Test for the well-balanced property of the 1D isothermal equilibrium

In this example, we will demonstrate that our scheme can maintain the isothermal

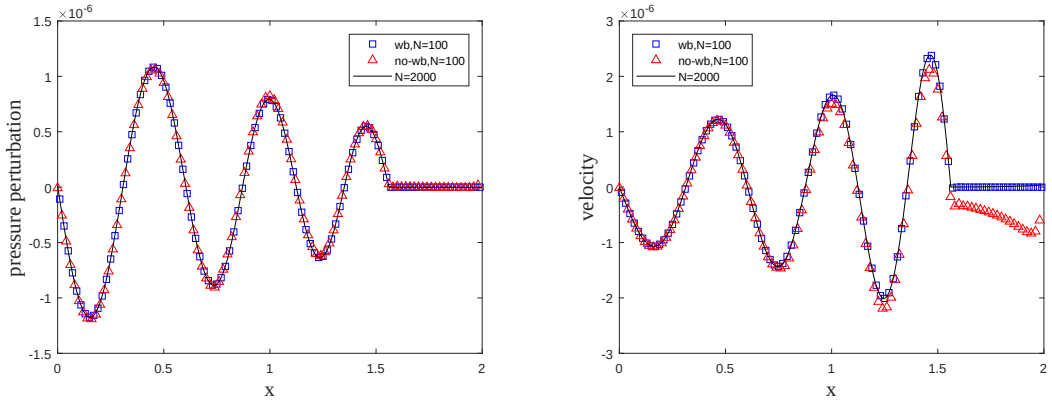

(a) Pressure perturbation (b) Velocity

Figure 3: Example 5.4: The comparison of numerical solution with small amplitude waves $A=10^{-6}$ and 100 cells at $T=1.5$.

Table 6: Example 5.5, L^1 errors for the isothermal equilibrium with different precisions.

N	precision	ρ	ρu	E
100	double	1.24E-14	6.88E-15	4.70E-14
	quadruple	7.03E-33	5.67E-33	1.63E-32
200	double	1.29E-14	6.74E-15	3.37E-14
	quadruple	2.45E-32	1.38E-32	1.11E-31

equilibrium state exactly. We consider the following isothermal equilibrium

$$\begin{aligned} \rho(x) &= \exp(-x), \\ u(x) &= 0, \\ p(x) &= \exp(-x), \end{aligned} \tag{5.4}$$

on a computational domain $[0,1]$ with $\gamma=1.4$ and gravitational field $\phi(x)=x$. The stop time is set as $T=2$. The L^1 errors of the numerical solutions with different precisions are shown in Table 6. It can be observed that our scheme maintains the equilibrium state with a round-off error, and this confirms its well-balanced property.

Example 5.6. Rarefaction test with low density and low pressure.

In this test, we consider an extreme rarefaction test to demonstrate that our scheme can keep the density and pressure positive. The initial condition is a Riemann problem given by

$$\rho=7, \quad p=0.2, \quad u=\begin{cases} -1 & x<0, \\ 1 & x>0, \end{cases}$$

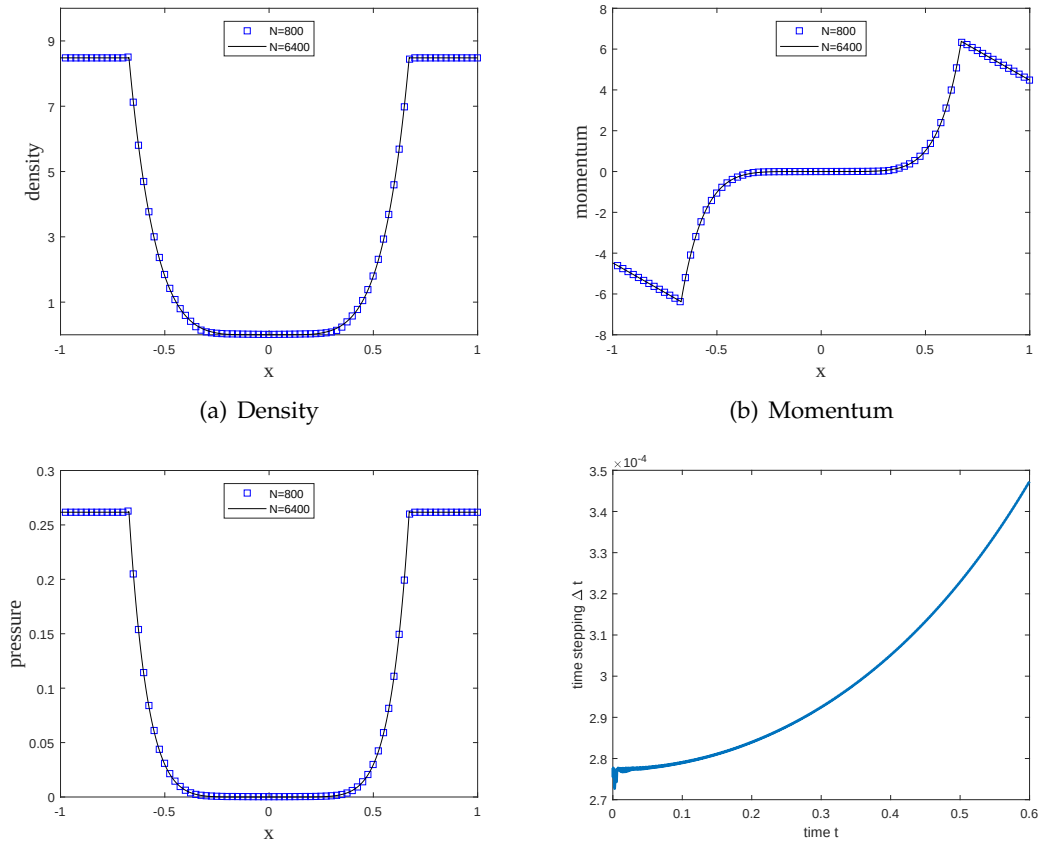

(a) Density (b) Momentum

(c) Pressure (d) Time stepping size Δt

Figure 4: Example 5.6, numerical solutions at $T=0.6$ with 800 cells (blue squares) and 6400 cells (black solid lines). Bottom right is the figure of time stepping size Δt versa time $t\in[0,0.6]$.

with $\gamma=1.4$ on the computational domain $[-1,1]$, and the gravitation field $\phi=x^2/2$ is considered. The outflow boundary conditions are imposed at both ends. The final time is set $T=0.6$ and 800 uniform cells are used. We choose the isothermal equilibrium recovery in this example. The numerical solutions at the final time are shown in Fig. 4, and we also include the reference solutions obtained with refined 6400 cells for comparison. We can see that the low pressure and the low density are both captured well by our methods. We also show the time stepping size at each time in the simulation in Fig. 4. We can see that our scheme can maintain sufficiently large time stepping size, which is similar to the standard DG scheme, in the whole simulation even the numerical solution involves low density and pressure. The minimum of density and pressure are shown in Table 7, which are indeed greater than 0.

Table 7: Example 5.6, the minimums of density and pressure for rarefaction test.

N	800	6400
ρ	9.95E-03	1.89E-03
p	2.89E-04	2.84E-05

5.2 Numerical examples in two dimensions

Example 5.7. Test for the accuracy in two dimensions.

In this example, we test the orders of accuracy in two-dimensional case when the triangular meshes are used. We consider the exact solution given by

$$\begin{aligned}
&\rho(x,y,t)=1+0.2\sin(\pi(x+y-2t)),\\
&u(x,y,t)=1,\\
&v(x,y,t)=1,\\
&p(x,y,t)=4.5+2t-x-y+0.2\cos(\pi(x+y-2t))/\pi,
\end{aligned}$$

on a square domain $[0,2]\times[0,2]$ with the gravitational field satisfying $\phi_x=\phi_y=1$ and $\gamma=1.4$. We apply the exact solutions at the boundaries. We set the stop time as $T=0.1$. We choose the isothermal equilibrium recovery in this example. Both the $\mathbb{P}^1$ and $\mathbb{P}^2$ piecewise polynomials are considered. The L^1 errors and the corresponding orders are shown in Table 8, from which we can see that our scheme have the desired high order accuracy.

Table 8: Example 5.7, two dimensional L^1 errors and orders of accuracy.

$k=1$	ρ		ρu		ρv		E	
N	L^1 error	order	L^1 error	order	L^1 error	order	L^1 error	order
200	2.70E-03	-	2.65E-03	-	2.65E-03	-	2.98E-03	-
800	6.76E-04	2.00	6.65E-04	1.99	6.65E-04	1.99	7.41E-04	2.01
3200	1.68E-04	2.00	1.66E-04	2.00	1.65E-04	2.00	1.84E-04	2.01
12800	4.21E-05	2.00	4.14E-05	2.00	4.14E-05	2.00	4.58E-05	2.00
$k=2$	ρ		ρu		ρv		E	
N	L^1 error	order	L^1 error	order	L^1 error	order	L^1 error	order
200	1.13E-04	-	1.14E-04	-	1.14E-04	-	1.01E-04	-
800	1.64E-05	2.79	1.63E-05	2.80	1.63E-05	2.80	1.50E-05	2.75
3200	2.19E-06	2.90	2.18E-06	2.91	2.18E-06	2.91	2.06E-06	2.86
12800	2.82E-07	2.96	2.80E-07	2.96	2.80E-07	2.96	2.70E-07	2.93

Example 5.8. Test for the well-balanced property of the 2D polytropic equilibrium.

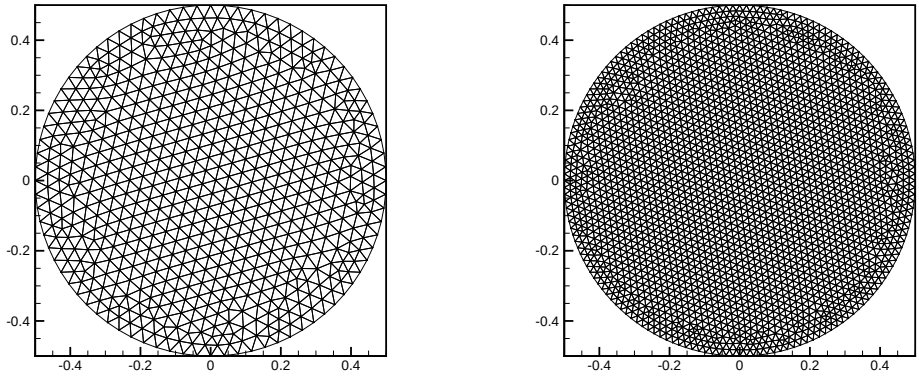

Figure 5: Example 5.8, the triangular meshes. Left: 1222 triangles for the well-balanced test; Right: 4826 triangles for the small perturbation test.

Table 9: Example 5.8, L^1 errors for the 2D polytropic equilibrium with different precisions on triangular meshes.

precision	L^1 error			
	ρ	ρu	ρv	E
double	9.21E-16	1.10E-15	1.25E-15	2.12E-16
quadruple	9.36E-34	1.19E-33	1.20E-33	2.04E-34

This example is used to verify that our scheme can maintain the polytropic equilibrium for 2D Euler equations. We take $\gamma=2$ and consider the polytropic equilibrium given by

$$\begin{aligned}\rho(r)&=\frac{\sin(\alpha r)}{\alpha r},\\ u(r)&=0,\\ v(r)&=0,\\ p(r)&=\rho(r)^2,\end{aligned}$$

with $r=\sqrt{x^2+y^2}$ and $\alpha=\sqrt{2\pi}$. The gravitational field $\phi(r)=-\frac{2\sin(\alpha r)}{\alpha r}$ is considered. Since this equilibrium state is axisymmetric, the computational domain is set as a disk centered at $(0,0)$ with radius 0.5. We choose a mesh with 1222 unstructured triangles as shown in the left part of Fig. 5. We set the stop time $T=2$. The L^1 errors of the numerical solutions with different precisions are shown in Table 9. It can be observed that our scheme maintains the polytropic equilibrium state with a round-off error, and this confirms its well-balanced property.

Next we impose a small perturbation to the polytropic equilibrium and test the capability of our scheme in capturing the propagation of the small perturbation. A small

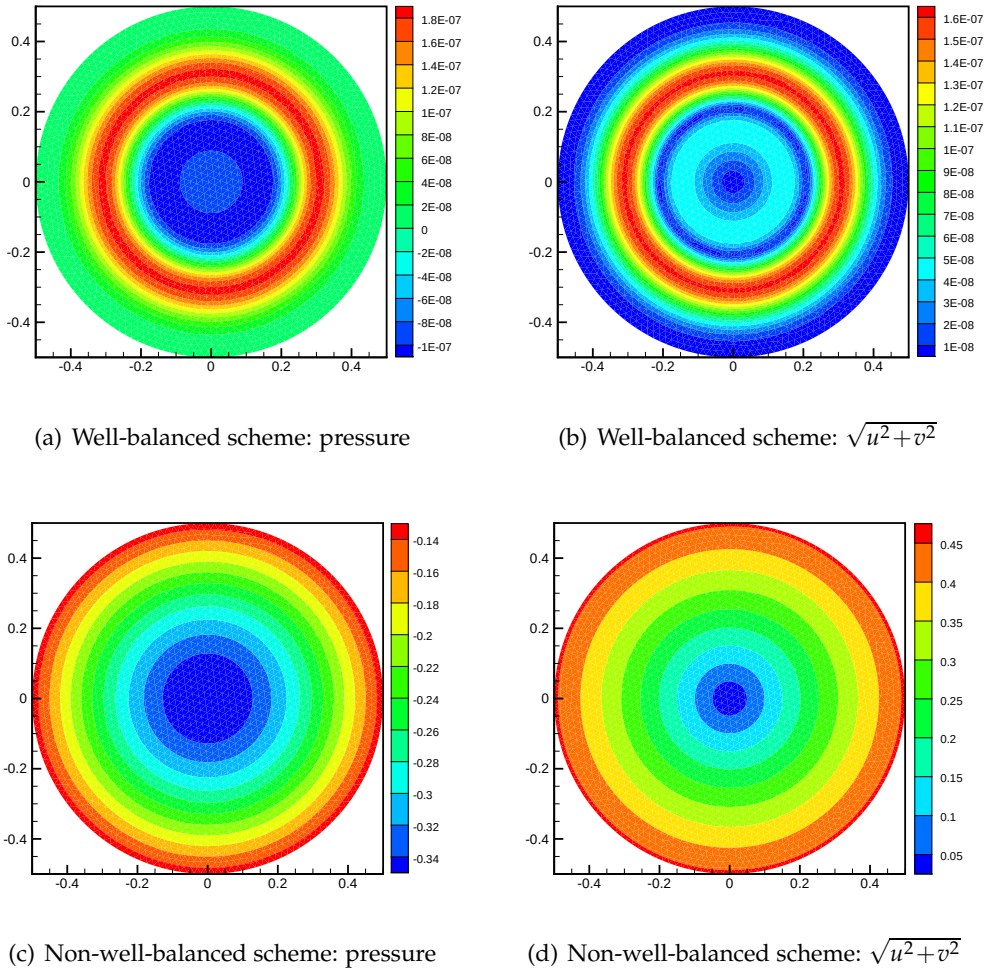

(a) Well-balanced scheme: pressure

(b) Well-balanced scheme: $\sqrt{u^2+v^2}$

(c) Non-well-balanced scheme: pressure

(d) Non-well-balanced scheme: $\sqrt{u^2+v^2}$

Figure 6: Example 5.8, contour plots of the numerical results on 4826 triangular cells at $t=0.2$.

Gaussian hump perturbation is added to the pressure such that

$$p(r)=\rho(r)^2+A\exp(-100r^2).$$

where the amplitude parameter A is set as 10^{-6}. The stop time is set as $T=0.2$. The computational domain is discretized by a mesh with 4826 triangles mesh, as shown in the right part of Fig. 5. We show the velocity and pressure perturbation of the well-balanced DG methods at the final time in Fig. 6. For comparison, we also show the results of the third order traditional non-WB DG method. We can observe that the well-balanced DG method can capture the small perturbation well, while the solutions of the non-WB method produces the non-physical wave with a much larger amplitude.

Example 5.9. Test for the well-balanced property of the 2D isothermal equilibrium.

In this example, we aim to preserve the isothermal equilibrium, which takes the form

$$\rho(x,y)=\rho_0\exp\Big(-\frac{\rho_0 g}{p_0}(x+y)\Big),\quad \boldsymbol{u}=0,\quad p(x,y)=p_0\exp\Big(-\frac{\rho_0 g}{p_0}(x+y)\Big),$$

with $\rho_0=1.21$, $p_0=1$ and $\gamma=1.4$. The gravitational field is given by $\phi(x,y)=g(x+y)$ with $g=1$. The computational domain is set as $\Omega=[0,1]^2$, which is discretized by 800 triangular meshes. We set the stop time $T=5$. The L^1 errors of the numerical solutions with different precisions are shown in Table 10. It can be observed that our scheme maintains the equilibrium state with a round-off error, and this confirms its well-balanced property.

Table 10: Example 5.9, L^1 errors for the 2D isothermal equilibrium with different precisions on triangular meshes.

precision	L^1 error			
	ρ	ρu	ρv	E
double	6.26E-16	9.67E-16	9.38E-16	9.16E-16
quadruple	5.56E-34	8.74E-34	9.33E-34	7.91E-34

Next, we impose a small perturbation to the isothermal equilibrium and test the capability of our scheme in capturing the propagation of the small perturbation. A small Gaussian hump perturbation is added to the pressure such that

$$p(x,y)=\frac{p_0}{\rho_0}\rho(x,y)+\epsilon\exp(-121((x-0.3)^2+(y-0.3)^2)).$$

where the amplitude parameter ϵ is set as 10^{-3}. The stop time is set as $T=0.15$ on 12800 triangular meshes. The numerical solutions of both well-balanced and non-WB methods are provided in Fig. 7, which shows that our numerical solution capture the propagation of the small perturbation correctly.

Example 5.10. Rarefaction test with low density and low pressure in two dimensions.

We use this 2D example to demonstrate the positivity-preserving property of the proposed DG method. We follow the 1-2-3 rarefaction test in [37], and consider the initial condition given by

$$\rho(x,y)=\exp(-2.5\phi(x,y)),\quad p(x,y)=0.4\exp(-2.5\phi(x,y))$$
$$u(x,y)=\begin{cases}-2 & x<0.5,\\ 2 & x>0.5,\end{cases},\qquad v(x,y)=0,$$

with the gravitational field $\phi(x,y)=\frac{1}{2}((x-0.5)^2+(y-0.5)^2)$ on the domain $\Omega=[0,1]^2$. Transmissive boundary conditions are considered. The computational domain is discretized by 12800 triangular meshes, and the stop time is set as $T=0.1$. We choose the

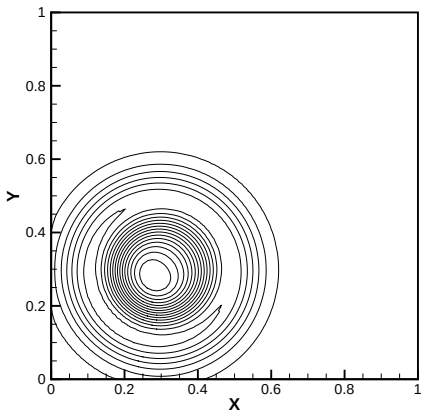

(a) Well-balanced scheme: pressure

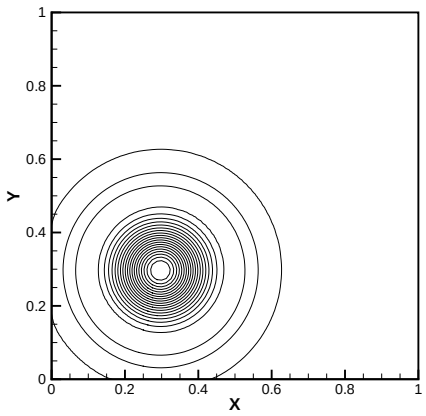

(b) Well-balanced scheme: density

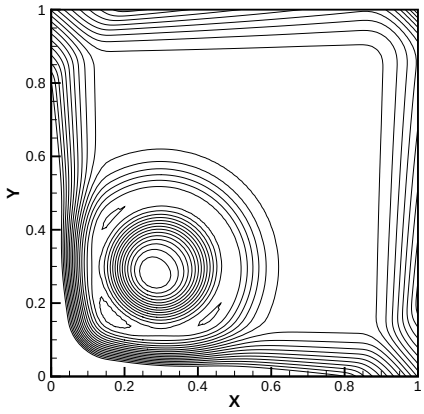

(c) Non-well-balanced scheme: pressure

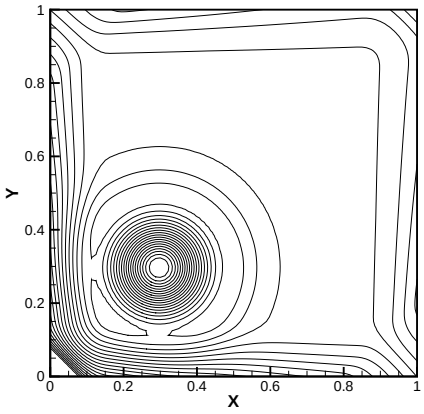

(d) Non-well-balanced scheme: density

Figure 7: Example 5.9, perturbation on the isothermal hydrostatic solution with $\epsilon=0.001$ at time $t=0.15$. Left: the pressure perturbation with 20 uniformly spaced contour lines from -0.0003 to 0.0003; Right: the density perturbation with 20 uniformly spaced contour lines from -0.001 to 0.0002.

CFL number to be 0.03. The numerical solutions of density, pressure and velocity at the final time are shown in Fig. 8. The minimum of density ρ is 5.35E-03 and the minimum of pressure p is 3.44E-03 at time $T=0.1$. We choose the isothermal equilibrium recovery in this example. We can observe that the low pressure and the low density are both captured well by our positivity-preserving DG methods. We show the time stepping size Δt versa time t in Fig. 8 and calculate the maximum of $\hat{\alpha}_1$ in (4.13) that

$$\max_{\forall K, t\leq 0.1} \hat{\alpha}_1 = 1.00126,$$

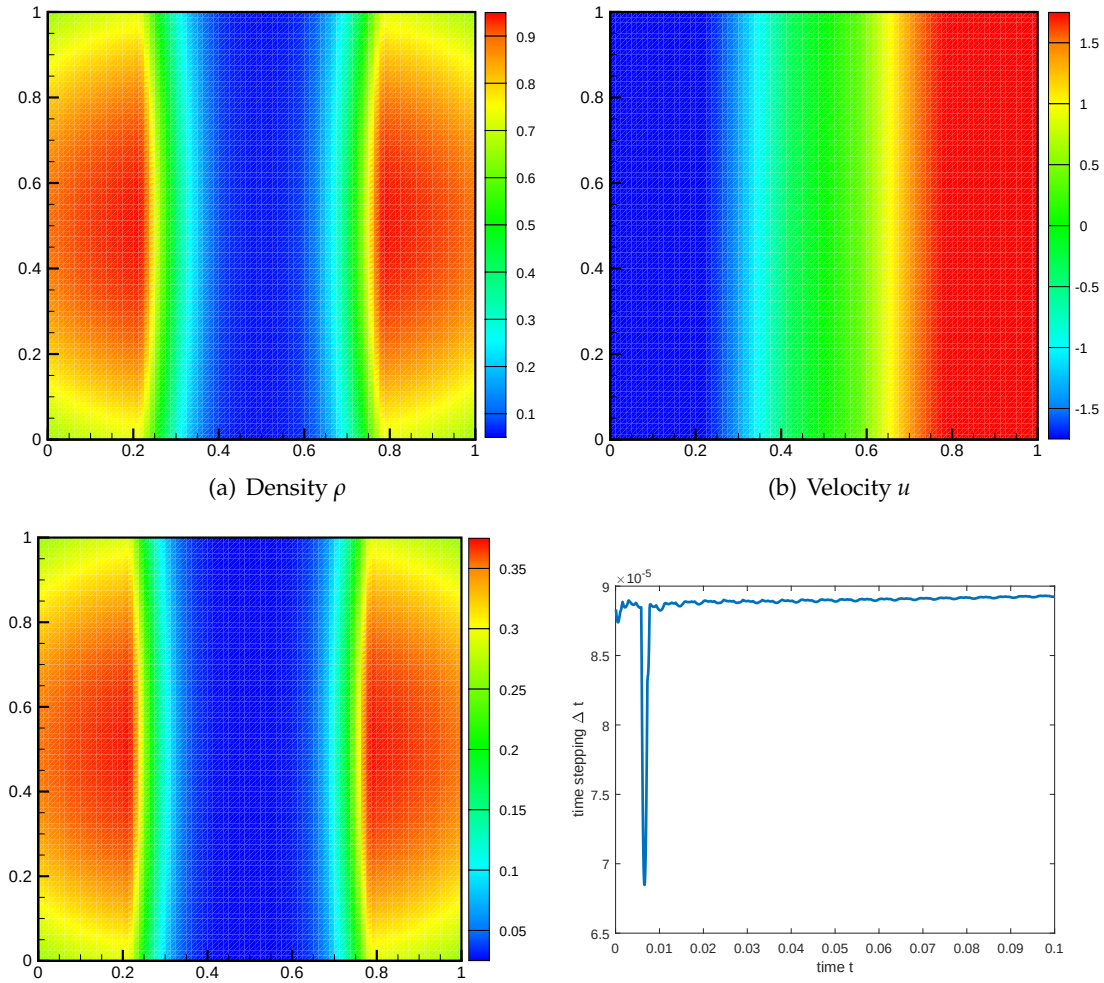

(a) Density ρ (b) Velocity u

(c) Pressure p (d) Time stepping size Δt

Figure 8: Example 5.10, numerical solutions by 12800 triangular meshes at $T=0.1$.

which means that the time stepping size of our proposed scheme is similar to the standard DG scheme and $\hat{\alpha}_1$ very close to constant 1 in the simulation.

Example 5.11. Inertia-gravity waves.

The inertia-gravity wave [19] is a two-dimensional benchmark for atmospheric models that involves the evolution of a potential temperature perturbation. Follow the setup, the domain is chosen to be 300000×10000. Periodic boundary conditions are applied on the left and right boundaries and inviscid wall boundary conditions are applied on the bottom and top boundaries. The initial flow is a perturbation added to a stratified

atmosphere in hydrostatic balanced background, and is given by

$$\begin{aligned}
&\rho(x,y)=\frac{p_0}{R\theta(x,y)}\left(1+\frac{(\gamma-1)g^2}{\gamma RT_0\mathcal{N}^2}\left(\exp\left(-\frac{\mathcal{N}^2}{g}y\right)-1\right)\right)^{\frac{1}{\gamma-1}},\\
&u(x,y)=20,\\
&v(x,y)=0,\\
&p(x,y)=p_0\left(1+\frac{(\gamma-1)g^2}{\gamma RT_0\mathcal{N}^2}\left(\exp\left(-\frac{\mathcal{N}^2}{g}y\right)-1\right)\right)^{\frac{\gamma}{\gamma-1}},
\end{aligned}$$

where the reference pressure and temperature at $y=0$ are $p_0=10^5$ and $T_0=300$, the buoyancy frequency $\mathcal{N}=0.01$, the gravitational force $g=9.8$, universal gas constant $R=287.058$ and $\gamma=1.4$. The potential temperature θ takes the form

$$\theta(x,y)=\theta_0+\Delta\theta(x,y),$$

where $\theta_0=T_0\exp(\frac{\mathcal{N}^2}{g}y)$,

$$\Delta\theta(x,y)=\theta_c\sin\left(\frac{\pi y}{h_c}\right)\left(1+\left(\frac{x-x_c}{a_c}\right)^2\right)^{-1},$$

with $\theta_c=0.01$, $h_c=10000$, $a_c=5000$, $x_c=100000$ and π being the Archimedes constant.

We simulate this problem up to $T=3000s$ on a grid of 30000 triangular meshes. We choose the polytropic equilibrium recovery in this example. Fig. 9 shows the potential temperature perturbation $\Delta\theta$ at different times $T=0,1000,2000,3000$. We observe that the evolution of potential temperature perturbation is correctly resolved, and they agree well with the results in [19].

Example 5.12. A shock wave diffracts at a convex corner.

A shock wave diffracting at a sharp convex corner [16, 50] is a classical benchmark problem in computational fluid dynamics. When the Mach number of the shock wave becomes larger, low density or pressure may appear. In this example, we study a Mach 10 shock diffracting at a 120° convex corner. We choose uniform right triangular meshes to discretize the domain, and use the shortest side of the triangular element to represent the mesh size. See Fig. 10 for the illustration of the computational domain with mesh size 17/30. The initial condition is a pure right moving shock with Mach 10, initially located at the boundary $x=3.4$ and $6\leq y\leq 11$, moving into an undisturbed air ahead of the shock with

$$\phi(x,y)=0.01x,\quad \rho(x,y)=1.4,\quad \boldsymbol{m}(x,y)=0,\quad p(x,y)=1.0476-\phi(x,y). \tag{5.5}$$

The boundary conditions are inflow at $x=3.4,6\leq y\leq 11$; outflow at $x=13.6,0\leq y\leq 11$ and $y=0,0\leq x\leq 13.6$ and $y=11,3.4\leq x\leq 13.6$; reflective at other boundaries. We choose the isothermal equilibrium recovery in this example.

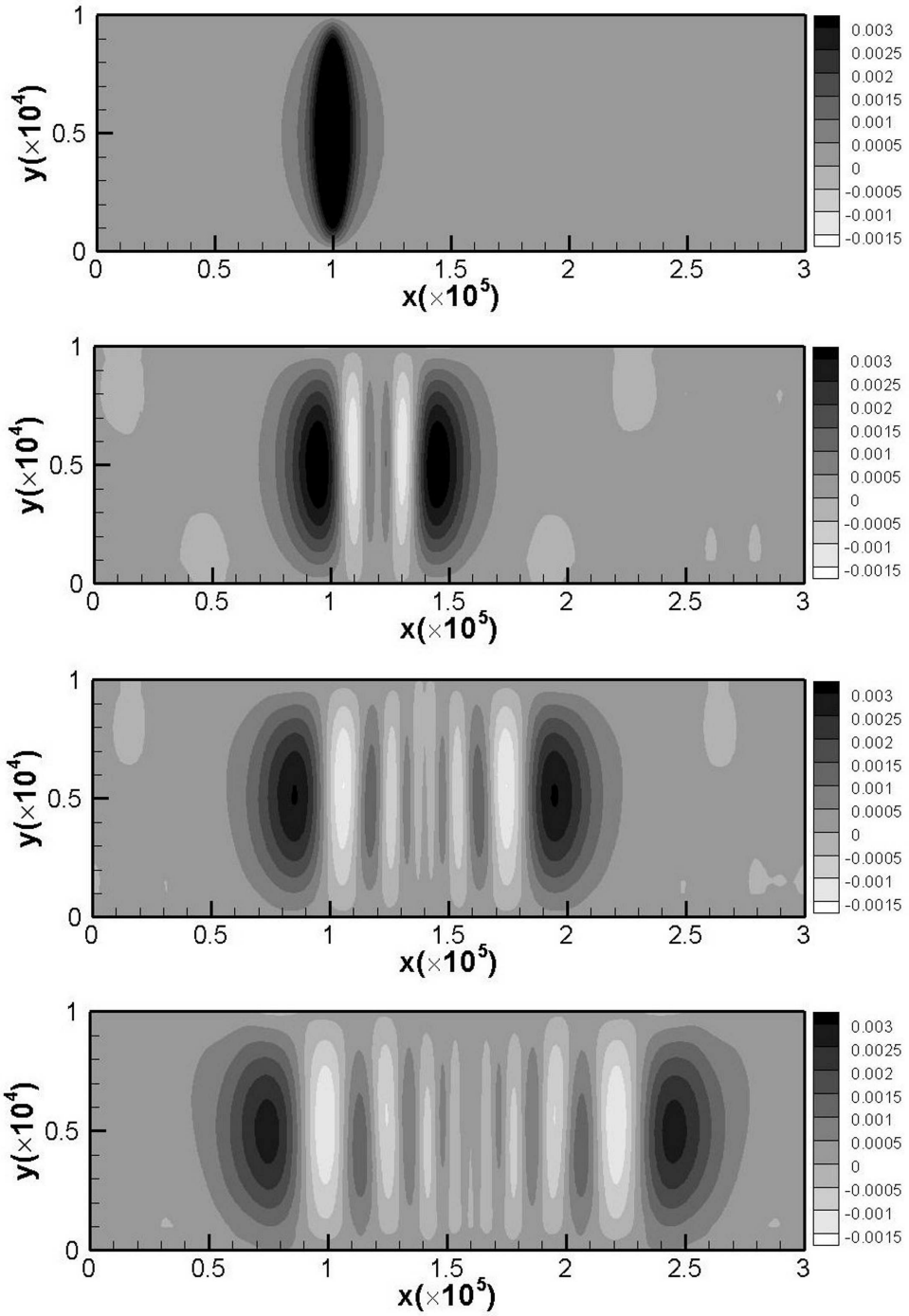

Figure 9: Example 5.11, potential temperature perturbation contour plots at time $T=0,1000,2000,3000$ (from top to bottom).

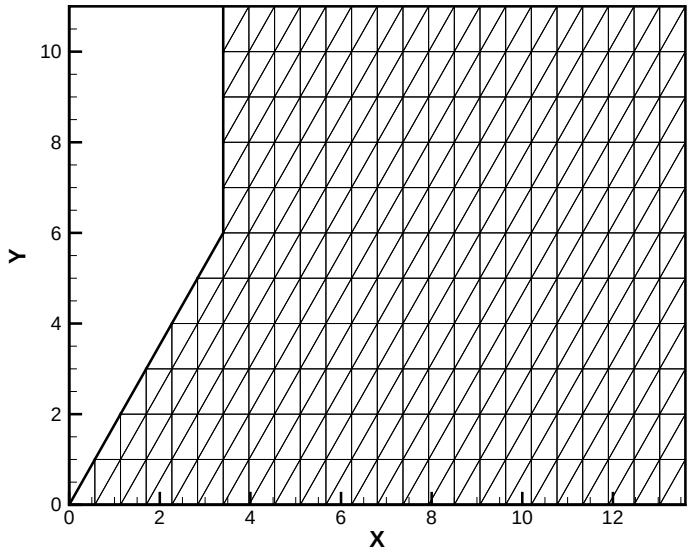

Figure 10: Example 5.12, the computational domain with triangular meshes of size 17/30.

Table 11: Example 5.12, the minimums of density and pressure for three different mesh sizes.

mesh size	$\frac{17}{300}$	$\frac{17}{600}$	$\frac{17}{1200}$
ρ	0.0144	0.0841	0.0947
p	1.73E-03	6.08E-04	8.27E-06

Our proposed DG scheme exhibits good robustness in the whole simulation. The density and pressure generated by the positivity-preserving DG methods at time $T=0.9$ are plotted in Fig. 11, with three different mesh sizes (of 17/300, 17/600 and 17/1200, respectively). We also report the minimal values of the density and pressure in Table 11. These numerical results are very consistent with the previous study in [50], and the proposed positivity-preserving limiter works well to maintain the positivity of the density and pressure.

6 Conclusion

In this paper, we developed the positivity-preserving well-balanced DG methods for the Euler equations with gravitation on triangular meshes. Our methods can preserve the polytropic and the isothermal equilibrium state. A modified LF well-balanced numerical flux together with a novel source term approximation are introduced to ensure the high order accuracy and the well-balanced property of the proposed methods. We also prove that our well-balanced scheme enjoys a weak positivity property, which implies that a scaling existing limiter can enforce the positivity-preserving property without los-

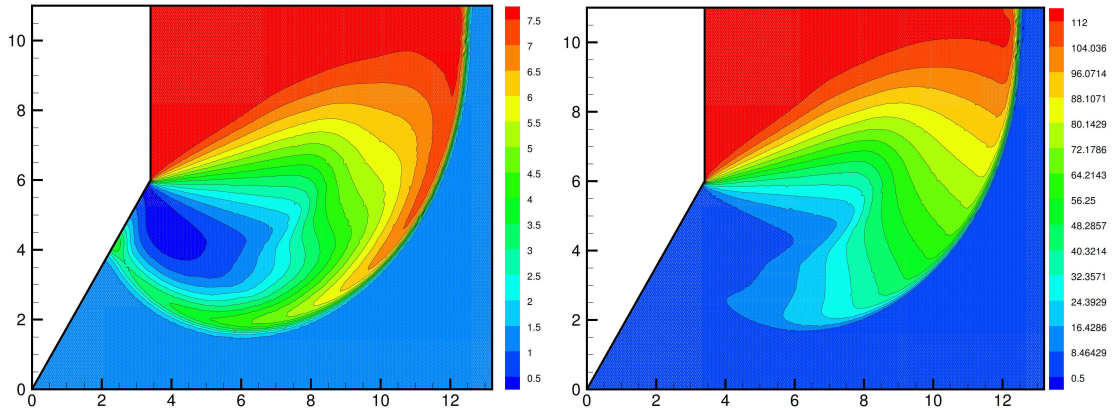

(a) density: mesh size 17/300 (b) pressure: mesh size 17/300

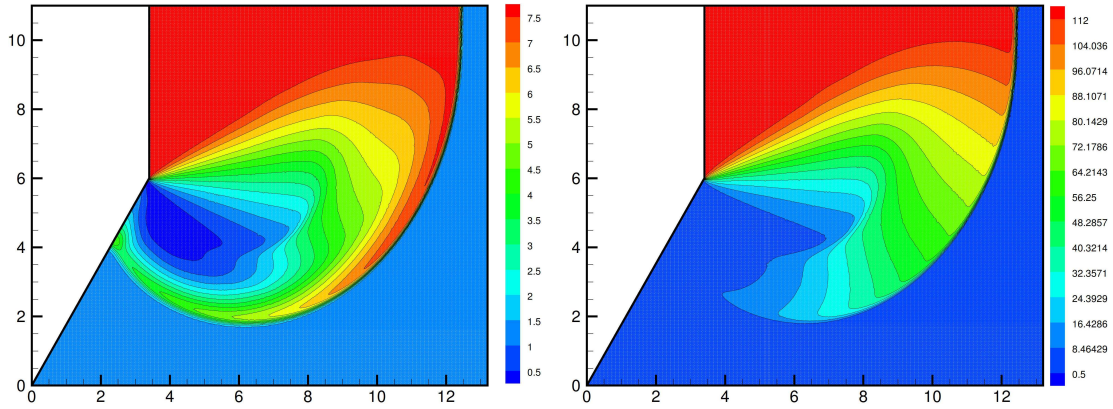

(c) density: mesh size 17/600 (d) pressure: mesh size 17/600

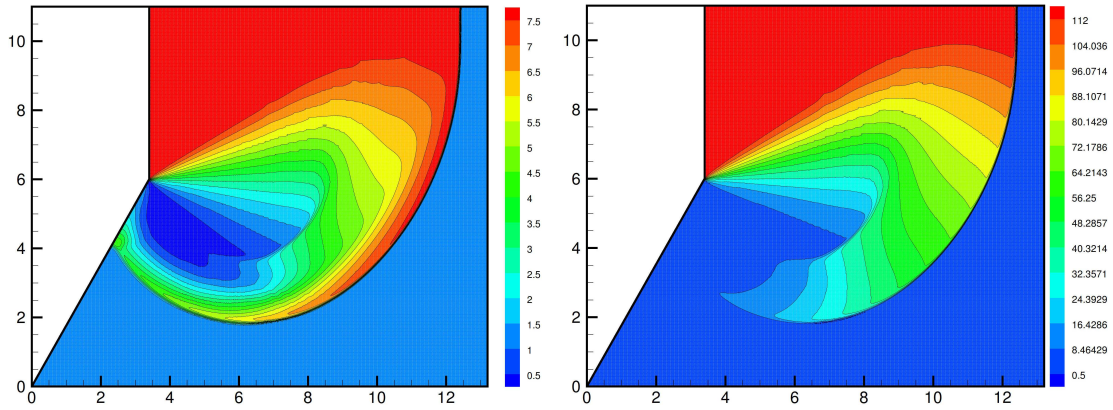

(e) density: mesh size 17/1200 (f) pressure: mesh size 17/1200

Figure 11: Example 5.12, 15 uniform contour plots of density from 0.5 to 7.5 and pressure from 0.5 to 112 at time $T=0.9$.

ing conservation and high-order accuracy. Moreover, our scheme is presented based on the triangular meshes. Both 1D and 2D numerical examples were provided to demonstrate the good features of our scheme. We plan to explore the extension of the proposed methods in the moving mesh framework in the future.

Acknowledgments

The work of W. Zhang was carried out when he was visiting Department of Mathematics, The Ohio State University under the support of the China Scholarship Council (CSC NO. 201906340196). The work of Y. Xing is partially supported by the NSF grant DMS-1753581. Research of Y. Xia is supported by NSFC grant No. 11871449. Research of Y. Xu is supported by National Numerical Windtunnel Project NNW2019ZT4-B08, NSFC grant No. 12071455, 11722112.

Appendices

A Proof for Lemma 4.4

Following the definition of α_0 and α_1, one can conclude that

$$1-\eta\frac{\rho^*}{\rho}\boldsymbol{u}\cdot\boldsymbol{n}>1-\eta\alpha_0|\boldsymbol{u}\cdot\boldsymbol{n}|>1-\frac{1}{\alpha_1}|\boldsymbol{u}\cdot\boldsymbol{n}|>0,$$
$$1-\eta\frac{p^*}{p}\boldsymbol{u}\cdot\boldsymbol{n}>1-\eta\alpha_0|\boldsymbol{u}\cdot\boldsymbol{n}|>1-\frac{1}{\alpha_1}|\boldsymbol{u}\cdot\boldsymbol{n}|>0.$$

Therefore, the first component of the vector in (4.6) stays positive since

$$\rho-\eta\boldsymbol{m}^*\cdot\boldsymbol{n}=\left(1-\eta\frac{\rho^*}{\rho}\boldsymbol{u}\cdot\boldsymbol{n}\right)\rho>0,$$

by utilizing the assumption $\boldsymbol{u}=\boldsymbol{u}^*$. Next, we show that the pressure is also positive, which follows from the following derivation:

$$\begin{aligned}\mathcal{G}(\boldsymbol{U}-\eta\boldsymbol{F}(\boldsymbol{U}^*)\cdot\boldsymbol{n})&=E-\eta(E^*\boldsymbol{u}^*+p^*\boldsymbol{u}^*)\cdot\boldsymbol{n}-\frac{1}{2}\frac{\|\boldsymbol{m}-\eta((\boldsymbol{u}^*\cdot\boldsymbol{n})\boldsymbol{m}^*+p^*\boldsymbol{n})\|^2}{\rho-\eta\rho^*\boldsymbol{u}^*\cdot\boldsymbol{n}}\\&=\frac{p}{\gamma-1}+\frac{1}{2}\rho\|\boldsymbol{u}\|^2-\eta\left(\left(\frac{p^*}{\gamma-1}+\frac{1}{2}\rho^*\|\boldsymbol{u}\|^2\right)\boldsymbol{u}+p^*\boldsymbol{u}\right)\cdot\boldsymbol{n}-\frac{1}{2}\frac{\|\rho\boldsymbol{u}-\eta(\boldsymbol{u}\cdot\boldsymbol{n})\rho^*\boldsymbol{u}-\eta p^*\boldsymbol{n}\|^2}{\rho-\eta\rho^*\boldsymbol{u}\cdot\boldsymbol{n}}\end{aligned}$$

$$
\begin{aligned}
&=\rho e+\frac{1}{2}\rho\|\boldsymbol{u}\|^2-\eta\boldsymbol{u}\cdot\boldsymbol{n}\left(\frac{p^*}{p}\rho e+\frac{1}{2}\frac{\rho^*}{\rho}\rho\|\boldsymbol{u}\|^2+p^*\right)\\
&\quad-\frac{(\rho-\eta\rho^*\boldsymbol{u}\cdot\boldsymbol{n})^2\|\boldsymbol{u}\|^2-2\eta(\rho-\eta\rho^*\boldsymbol{u}\cdot\boldsymbol{n})p^*\boldsymbol{u}\cdot\boldsymbol{n}+\eta^2(p^*)^2}{2(\rho-\eta\rho^*\boldsymbol{u}\cdot\boldsymbol{n})}\\
&=\rho e\left(1-\eta\frac{p^*}{p}\boldsymbol{u}\cdot\boldsymbol{n}\right)+\frac{1}{2}\rho\|\boldsymbol{u}\|^2\left(1-\eta\frac{\rho^*}{\rho}\boldsymbol{u}\cdot\boldsymbol{n}\right)-\eta p^*\boldsymbol{u}\cdot\boldsymbol{n}\\
&\quad-\frac{1}{2}\rho\|\boldsymbol{u}\|^2\left(1-\eta\frac{\rho^*}{\rho}\boldsymbol{u}\cdot\boldsymbol{n}\right)+\eta p^*\boldsymbol{u}\cdot\boldsymbol{n}-\frac{\eta^2(p^*)^2}{2(\rho-\eta\rho^*\boldsymbol{u}\cdot\boldsymbol{n})}\\
&=\rho e\left(1-\eta\frac{p^*}{p}\boldsymbol{u}\cdot\boldsymbol{n}-\frac{\eta^2(p^*)^2}{2\left(1-\eta\frac{\rho^*}{\rho}\boldsymbol{u}\cdot\boldsymbol{n}\right)\rho^2e}\right)>\rho e\left(1-\frac{1}{\alpha_1}|\boldsymbol{u}\cdot\boldsymbol{n}|-\frac{(\eta\alpha_0 p)^2}{2\left(1-\frac{1}{\alpha_1}|\boldsymbol{u}\cdot\boldsymbol{n}|\right)\rho^2e}\right)\\
&>\rho e\left(1-\frac{1}{\alpha_1}|\boldsymbol{u}\cdot\boldsymbol{n}|-\frac{\left(\frac{1}{\alpha_1}p\right)^2}{2\left(1-\frac{1}{\alpha_1}|\boldsymbol{u}\cdot\boldsymbol{n}|\right)\rho^2e}\right)\\
&=\frac{\rho e}{2\left(1-\frac{1}{\alpha_1}|\boldsymbol{u}\cdot\boldsymbol{n}|\right)\rho^2e}\left(2\left(1-\frac{1}{\alpha_1}|\boldsymbol{u}\cdot\boldsymbol{n}|\right)^2\rho^2e-\left(\frac{1}{\alpha_1}p\right)^2\right)\\
&=0,
\end{aligned}
$$

where we again use the assumption that $\boldsymbol{u}=\boldsymbol{u}^*$. The last equality follows from the definition of α_1 which leads to

$$1-\frac{1}{\alpha_1}|\boldsymbol{u}\cdot\boldsymbol{n}|=\frac{1}{\alpha_1}\frac{p}{\rho\sqrt{2e}}.$$

Therefore we can conclude (4.6) and this finishes the proof. □

B Proof for Proposition 4.1

Since the SSP Runge-Kutta methods can be written as the convex combination of the forward Euler methods, we only need to prove the result for the semi-discrete scheme (3.17) coupled with forward Euler time discretization, which takes the form

$$\int_K \boldsymbol{U}_K^{n+1}\cdot\boldsymbol{\varphi}\mathrm{d}\boldsymbol{x}=\int_K \boldsymbol{U}_K^{n}\cdot\boldsymbol{\varphi}\mathrm{d}\boldsymbol{x}+\Delta t\boldsymbol{\mathcal{L}}_K(\boldsymbol{U}^n),\tag{B.1}$$

with $\boldsymbol{\mathcal{L}}_K(\boldsymbol{U}^n)$ defined in (3.18).

By taking the test function $\boldsymbol{\varphi}=1$, one can obtain the equation satisfied by $\bar{\boldsymbol{U}}_K^{n+1}$, which

can be further decomposed into two parts as follows:

$$\begin{aligned}\bar{\boldsymbol{U}}_K^{n+1} &= \bar{\boldsymbol{U}}_K^n + \lambda\left(-\int_{\partial K}\hat{\boldsymbol{F}}\left(\boldsymbol{U}^{b,int_K},\boldsymbol{U}^{b,ext_K},\boldsymbol{n}\right)\mathrm{d}\boldsymbol{s}\right.\\ &\qquad\left.+\int_K \boldsymbol{S}\left(\boldsymbol{U}^f,-\frac{\nabla p^{\tilde{e}}}{\rho^e}\right)\mathrm{d}\boldsymbol{x}+\int_{\partial K}\boldsymbol{F}\left(\boldsymbol{U}^{\tilde{e},int_K}\right)\cdot\boldsymbol{n}\mathrm{d}\boldsymbol{s}\right)\\ &= \boldsymbol{W}_1+\boldsymbol{W}_2,\end{aligned}$$

with

$$\boldsymbol{W}_1 = \zeta\bar{\boldsymbol{U}}_K^n - \lambda\int_{\partial K}\hat{\boldsymbol{F}}\left(\boldsymbol{U}^{b,int_K},\boldsymbol{U}^{b,ext_K},\boldsymbol{n}\right)\mathrm{d}\boldsymbol{s}, \tag{B.2}$$

$$\boldsymbol{W}_2 = \vartheta\bar{\boldsymbol{U}}_K^n + \lambda\left(\int_K \boldsymbol{S}\left(\boldsymbol{U}^f,-\frac{\nabla p^{\tilde{e}}}{\rho^e}\right)\mathrm{d}\boldsymbol{x}+\int_{\partial K}\boldsymbol{F}\left(\boldsymbol{U}^{\tilde{e},int_K}\right)\cdot\boldsymbol{n}\mathrm{d}\boldsymbol{s}\right), \tag{B.3}$$

where

$$\zeta = \frac{\hat{\alpha}_F}{\hat{\alpha}_0},\quad \vartheta = \frac{\hat{\alpha}_S}{\hat{\alpha}_0},\qquad \text{satisfying } \zeta+\vartheta = 1, \tag{B.4}$$

and $\lambda = \frac{\Delta t}{\Delta_K}$. To show that $\bar{\boldsymbol{U}}_K^{n+1}\in G$, we only need to prove that $\boldsymbol{W}_1$, $\boldsymbol{W}_2\in G$, since G is a convex set.

- **Step 1: The proof of $\boldsymbol{W}_1\in G$.**

Since $\boldsymbol{U}_K^n$ are polynomials on K, we can rewrite the average $\bar{\boldsymbol{U}}_K^n$ as (4.10). Following quadrature rule (4.9) and the LF flux defined in (2.12), we can rewrite $\boldsymbol{W}_1$ as

$$\begin{aligned}\boldsymbol{W}_1 &= \frac{1}{2}\left(2\zeta\sum_{\nu=1}^{d+1}\sum_{\mu=1}^{N}\tilde{\omega}_{F_K^\nu}^\mu\boldsymbol{U}^{n,int_K}\left(\tilde{\boldsymbol{x}}_{F_K^\nu}^\mu\right)+2\zeta\sum_{\mu=1}^{\tilde{L}}\tilde{\omega}_K^\mu\boldsymbol{U}_K^n\left(\tilde{\boldsymbol{x}}_K^\mu\right)\right.\\ &\quad-\lambda\sum_{\nu=1}^{d+1}\sum_{\mu=1}^{N}\tilde{\omega}_{F_K^\nu}^\mu|F_K^\nu|\left(\boldsymbol{F}\left(\boldsymbol{U}^{b,int_K}\left(\tilde{\boldsymbol{x}}_{F_K^\nu}^\mu\right)\right)\cdot\boldsymbol{n}+\boldsymbol{F}\left(\boldsymbol{U}^{b,ext_K}\left(\tilde{\boldsymbol{x}}_{F_K^\nu}^\mu\right)\right)\cdot\boldsymbol{n}\right.\\ &\qquad\left.\left.-\alpha\boldsymbol{U}^{b,ext_K}\left(\tilde{\boldsymbol{x}}_{F_K^\nu}^\mu\right)+\alpha\boldsymbol{U}^{b,int_K}\left(\tilde{\boldsymbol{x}}_{F_K^\nu}^\mu\right)\right)\right)\\ &= \zeta\sum_{\mu=1}^{\tilde{L}}\tilde{\omega}_K^\mu\boldsymbol{U}_K^n\left(\tilde{\boldsymbol{x}}_K^\mu\right)\end{aligned}$$

$$
\begin{aligned}
&+\frac{\lambda}{2}\sum_{\nu=1}^{d+1}\sum_{\mu=1}^{N}\tilde{\omega}_{F_K^\nu}^{\mu}|F_K^\nu|\left(\alpha\boldsymbol{U}^{b,ext_K}\left(\tilde{\boldsymbol{x}}_{F_K^\nu}^{\mu}\right)-\boldsymbol{F}\left(\boldsymbol{U}^{b,ext_K}\left(\tilde{\boldsymbol{x}}_{F_K^\nu}^{\mu}\right)\right)\cdot\boldsymbol{n}\right.\\
&+\zeta\frac{\tilde{\omega}_{F_K^\nu}^{\mu}}{\lambda\tilde{\omega}_{F_K^\nu}^{\mu}|F_K^\nu|}\boldsymbol{U}^{n,int_K}\left(\tilde{\boldsymbol{x}}_{F_K^\nu}^{\mu}\right)-\alpha\boldsymbol{U}^{b,int_K}\left(\tilde{\boldsymbol{x}}_{F_K^\nu}^{\mu}\right)\\
&\left.+\zeta\frac{\tilde{\omega}_{F_K^\nu}^{\mu}}{\lambda\tilde{\omega}_{F_K^\nu}^{\mu}|F_K^\nu|}\boldsymbol{U}^{n,int_K}\left(\tilde{\boldsymbol{x}}_{F_K^\nu}^{\mu}\right)-\boldsymbol{F}\left(\boldsymbol{U}^{b,int_K}\left(\tilde{\boldsymbol{x}}_{F_K^\nu}^{\mu}\right)\right)\cdot\boldsymbol{n}\right)\\
=:&\ \mathrm{I}+\mathrm{II}+\mathrm{III}+\mathrm{IV},
\end{aligned}
$$

where $|F_K^\nu|$ denotes the area of edge F_K^ν. Since the admissible state G is convex and $\boldsymbol{W}_1$ is decomposed into four parts, the goal is now to prove that all of these four parts belong to G. Note that the parameters ζ, λ, $|F_K^\nu|$, and the quadrature weights $\tilde{\omega}_K^\mu$, $\tilde{\omega}_{F_K^\nu}^\mu$, $\tilde{\omega}_{F_K^\nu}^\mu$ are all positive, hence we only need to prove the following four claims:

1. $\boldsymbol{U}_K^n\left(\tilde{\boldsymbol{x}}_K^\mu\right)\in G$.

   This follows from the assumption that

   $$\boldsymbol{U}_K^n(\boldsymbol{x})\in G,\quad \text{for } \boldsymbol{x}\in\mathbb{S}_K.$$

2. $\alpha\boldsymbol{U}^{b,ext_K}\left(\tilde{\boldsymbol{x}}_{F_K^\nu}^\mu\right)-\boldsymbol{F}\left(\boldsymbol{U}^{b,ext_K}\left(\tilde{\boldsymbol{x}}_{F_K^\nu}^\mu\right)\right)\cdot\boldsymbol{n}\in G$.

   Using the definition of α in (2.13), we have

   $$\alpha>\left|\boldsymbol{u}^{b,ext_K}\cdot\boldsymbol{n}\right|+\sqrt{\gamma p^{b,ext_K}/\rho^{b,ext_K}}>\left|\boldsymbol{u}^{b,ext_K}\cdot\boldsymbol{n}\right|+\frac{p^{b,ext_K}}{\rho^{b,ext_K}\sqrt{2e^{b,ext_K}}},\tag{B.5}$$

   since $\frac{\gamma-1}{\gamma}=1-\frac{1}{\gamma}<2$ holds for any $\gamma\geq 1$. It indicates that $\eta=1/\alpha$ satisfies the constraints in (4.2). By utilizing Lemma 4.2 and the fact

   $$\boldsymbol{U}^{b,ext_K}\left(\tilde{\boldsymbol{x}}_{F_K^\nu}^\mu\right)\in G,$$

   we have

   $$\alpha\boldsymbol{U}^{b,ext_K}\left(\tilde{\boldsymbol{x}}_{F_K^\nu}^\mu\right)-\boldsymbol{F}\left(\boldsymbol{U}^{b,ext_K}\left(\tilde{\boldsymbol{x}}_{F_K^\nu}^\mu\right)\right)\cdot\boldsymbol{n}\in G.\tag{B.6}$$

3. $\zeta\frac{\tilde{\omega}_{F_K^\nu}^\mu}{\lambda\tilde{\omega}_{F_K^\nu}^\mu|F_K^\nu|}\boldsymbol{U}^{n,int_K}\left(\tilde{\boldsymbol{x}}_{F_K^\nu}^\mu\right)-\alpha\boldsymbol{U}^{b,int_K}\left(\tilde{\boldsymbol{x}}_{F_K^\nu}^\mu\right)\in G$.

Following the definition of $\hat{\alpha}_1$, $\hat{\alpha}_0$, $\hat{\alpha}_F$ in (4.13) and that of ζ in (B.4), we have

$$\begin{aligned}\zeta\frac{\tilde{\omega}^{\mu}_{F^{\nu}_K}}{\lambda\tilde{\omega}^{\mu}_{F^{\nu}_K}|F^{\nu}_K|}&=\frac{\hat{\alpha}_F}{\hat{\alpha}_0}\frac{\Delta_K\tilde{\omega}^{\mu}_{F^{\nu}_K}}{\Delta t\tilde{\omega}^{\mu}_{F^{\nu}_K}|F^{\nu}_K|}\geq\frac{\hat{\alpha}_1\alpha}{\hat{\alpha}_0\Delta t}\\&>\hat{\alpha}_1\alpha\geq\max\left(\frac{\rho^{b,int_K}\left(\tilde{\boldsymbol{x}}^{\mu}_{F^{\nu}_K}\right)}{\rho^{n,int_K}\left(\tilde{\boldsymbol{x}}^{\mu}_{F^{\nu}_K}\right)},\frac{p^{b,int_K}\left(\tilde{\boldsymbol{x}}^{\mu}_{F^{\nu}_K}\right)}{p^{n,int_K}\left(\tilde{\boldsymbol{x}}^{\mu}_{F^{\nu}_K}\right)}\right)\alpha,\end{aligned}\tag{B.7}$$

which leads to

$$\max\left(\frac{\rho^{b,int_K}\left(\tilde{\boldsymbol{x}}^{\mu}_{F^{\nu}_K}\right)}{\rho^{n,int_K}\left(\tilde{\boldsymbol{x}}^{\mu}_{F^{\nu}_K}\right)},\frac{p^{b,int_K}\left(\tilde{\boldsymbol{x}}^{\mu}_{F^{\nu}_K}\right)}{p^{n,int_K}\left(\tilde{\boldsymbol{x}}^{\mu}_{F^{\nu}_K}\right)}\right)\frac{\alpha\lambda\tilde{\omega}^{\mu}_{F^{\nu}_K}|F^{\nu}_K|}{\zeta\tilde{\omega}^{\mu}_{F^{\nu}_K}}<1.$$

This suggests that

$$\eta=\frac{\alpha\lambda\tilde{\omega}^{\mu}_{F^{\nu}_K}|F^{\nu}_K|}{\zeta\tilde{\omega}^{\mu}_{F^{\nu}_K}}$$

satisfies the constraints in (4.5). By combining Lemma 4.3 with the fact that

$$\boldsymbol{U}^{n,int_K}\left(\tilde{\boldsymbol{x}}^{\mu}_{F^{\nu}_K}\right),\ \boldsymbol{U}^{b,int_K}\left(\tilde{\boldsymbol{x}}^{\mu}_{F^{\nu}_K}\right)\in G,$$

we have

$$\zeta\frac{\tilde{\omega}^{\mu}_{F^{\nu}_K}}{\alpha\lambda\tilde{\omega}^{\mu}_{F^{\nu}_K}|F^{\nu}_K|}\boldsymbol{U}^{n,int_K}\left(\tilde{\boldsymbol{x}}^{\mu}_{F^{\nu}_K}\right)-\boldsymbol{U}^{b,int_K}\left(\tilde{\boldsymbol{x}}^{\mu}_{F^{\nu}_K}\right)\in G.$$

4. $\zeta\frac{\tilde{\omega}^{\mu}_{F^{\nu}_K}}{\lambda\tilde{\omega}^{\mu}_{F^{\nu}_K}|F^{\nu}_K|}\boldsymbol{U}^{n,int_K}\left(\tilde{\boldsymbol{x}}^{\mu}_{F^{\nu}_K}\right)-\boldsymbol{F}\left(\boldsymbol{U}^{b,int_K}\left(\tilde{\boldsymbol{x}}^{\mu}_{F^{\nu}_K}\right)\right)\cdot\boldsymbol{n}\in G.$

The combination of Eqs. (B.7) and (B.5) leads to

$$\zeta\frac{\tilde{\omega}^{\mu}_{F^{\nu}_K}}{\lambda\tilde{\omega}^{\mu}_{F^{\nu}_K}|F^{\nu}_K|}>\hat{\alpha}_1\alpha>\max\left(\frac{\rho^{b,int_K}}{\rho^{n,int_K}},\frac{p^{b,int_K}}{p^{n,int_K}}\right)\left(\left|\boldsymbol{u}^{n,int_K}\cdot\boldsymbol{n}\right|+\frac{p^{n,int_K}}{\rho^{n,int_K}\sqrt{2e^{n,int_K}}}\right)\Bigg|_{\tilde{\boldsymbol{x}}^{\mu}_{F^{\nu}_K}},$$

which indicates that

$$\eta=\frac{\lambda\tilde{\omega}^{\mu}_{F^{\nu}_K}|F^{\nu}_K|}{\zeta\tilde{\omega}^{\mu}_{F^{\nu}_K}}$$

satisfies the constraints in (4.7). By utilizing Lemma 4.4 and the fact

$$\boldsymbol{U}^{n,int_K}\left(\tilde{\boldsymbol{x}}^{\mu}_{F^{\nu}_K}\right),\ \boldsymbol{U}^{b,int_K}\left(\tilde{\boldsymbol{x}}^{\mu}_{F^{\nu}_K}\right)\in G,$$

we conclude that

$$\zeta\frac{\tilde{\omega}^{\mu}_{F^{\nu}_K}}{\lambda\tilde{\omega}^{\mu}_{F^{\nu}_K}|F^{\nu}_K|}\boldsymbol{U}^{n,int_K}\left(\tilde{\boldsymbol{x}}^{\mu}_{F^{\nu}_K}\right)-\boldsymbol{F}\left(\boldsymbol{U}^{b,int_K}\left(\tilde{\boldsymbol{x}}^{\mu}_{F^{\nu}_K}\right)\right)\cdot\boldsymbol{n}\in G.$$

The combination of all the claims above yields the conclusion that $\boldsymbol{W}_1\in G$.

- **Step 2: The proof of $\boldsymbol{W}_2\in G$.**

Notice that $\boldsymbol{m}^{\tilde{e},int_K}\equiv 0$ and

$$\boldsymbol{F}\left(\boldsymbol{U}^{\tilde{e},int_K}\right)=\begin{pmatrix}0\\(\gamma-1)E^{\tilde{e},int_K}\boldsymbol{I}_d\\0\end{pmatrix},$$

which suggests that every component of $\boldsymbol{F}\left(\boldsymbol{U}^{\tilde{e},int_K}\right)$ is a polynomial in ∂K. Therefore it can be exactly integrated by the quadrature rule (4.9), and one can use the integration by parts and the 2D quadrature rule (4.8) to rewrite $\boldsymbol{W}_2$ as

$$\begin{aligned}\boldsymbol{W}_2&=\vartheta\bar{\boldsymbol{U}}^n_K+\lambda\left(\int_K\boldsymbol{S}\left(\boldsymbol{U}^f,-\frac{\nabla p^{\tilde{e}}}{\rho^e}\right)\mathrm{d}\boldsymbol{x}+\int_K\nabla\cdot\boldsymbol{F}\left(\boldsymbol{U}^{\tilde{e}}\right)\mathrm{d}\boldsymbol{x}\right)\\&=\sum_{\mu=1}^{L}\hat{\omega}^{\mu}_K\left(\vartheta\boldsymbol{U}^n_K\left(\hat{\boldsymbol{x}}^{\mu}_K\right)+\Delta t\left(\nabla\cdot\boldsymbol{F}\left(\boldsymbol{U}^{\tilde{e}}_K\left(\hat{\boldsymbol{x}}^{\mu}_K\right)\right)+\boldsymbol{S}\left(\boldsymbol{U}^f_K\left(\hat{\boldsymbol{x}}^{\mu}_K\right),-\frac{\nabla p^{\tilde{e}}_K\left(\hat{\boldsymbol{x}}^{\mu}_K\right)}{\rho^e_K\left(\hat{\boldsymbol{x}}^{\mu}_K\right)}\right)\right)\right).\end{aligned}$$

Since G is convex and all the quadrature weights are positive, it is sufficient to prove, for $\mu=1,\cdots,L$,

$$\boldsymbol{W}^{\mu}_2=\vartheta\boldsymbol{U}^n_K\left(\hat{\boldsymbol{x}}^{\mu}_K\right)+\Delta t\left(\nabla\cdot\boldsymbol{F}\left(\boldsymbol{U}^{\tilde{e}}_K\left(\hat{\boldsymbol{x}}^{\mu}_K\right)\right)+\boldsymbol{S}\left(\boldsymbol{U}^f_K\left(\hat{\boldsymbol{x}}^{\mu}_K\right),-\frac{\nabla p^{\tilde{e}}_K\left(\hat{\boldsymbol{x}}^{\mu}_K\right)}{\rho^e_K\left(\hat{\boldsymbol{x}}^{\mu}_K\right)}\right)\right)\in G.$$

The first component of $\boldsymbol{W}^{\mu}_2$ reduces to $\vartheta\rho^n_K\left(\hat{\boldsymbol{x}}^{\mu}_K\right)$ which is automatically positive. In order to show that $\mathcal{G}\left(\boldsymbol{W}^{\mu}_2\right)>0$, we have

$$\mathcal{G}\left(\boldsymbol{W}^{\mu}_2\right)=\vartheta E^n_K+\Delta t\boldsymbol{m}^f_K\cdot\frac{\nabla p^{\tilde{e}}_K}{\rho^e_K}-\left.\frac{\left\|\vartheta\boldsymbol{m}^n_K+\Delta t\left(\nabla p^{\tilde{e}}_K+\rho^f_K\frac{\nabla p^{\tilde{e}}_K}{\rho^e_j}\right)\right\|^2}{2\vartheta\rho^n_K}\right|_{\hat{\boldsymbol{x}}^{\mu}_K}$$

$$
\begin{aligned}
&= \vartheta E_K^n + \Delta t \boldsymbol{m}_K^f \cdot \frac{\nabla p_K^{\tilde{e}}}{\rho_K^e} - \frac{\left\| \vartheta \boldsymbol{m}_K^n + \Delta t \frac{\rho_K^n}{\rho_K^e} \nabla p_K^{\tilde{e}} \right\|^2}{2\vartheta \rho_K^n} \Bigg|_{\hat{\boldsymbol{x}}_K^\mu} \\
&= \vartheta (\rho e)_K^n + \Delta t \boldsymbol{m}_K^f \cdot \frac{\nabla p_K^{\tilde{e}}}{\rho_K^e} - \Delta t \frac{\boldsymbol{m}_K^n}{\rho_K^e} \cdot \nabla p_K^{\tilde{e}} - \Delta t^2 \frac{\left\| \frac{\rho_K^n}{\rho_K^e} \nabla p_K^{\tilde{e}} \right\|^2}{2\vartheta \rho_K^n} \Bigg|_{\hat{\boldsymbol{x}}_K^\mu} \\
&= \vartheta (\rho e)_K^n \left(1 - \Delta t^2 \frac{\left\| \nabla p_K^{\tilde{e}} / \rho_K^e \right\|^2}{2\vartheta^2 e_K^n} \right) \Bigg|_{\hat{\boldsymbol{x}}_K^\mu},
\end{aligned}
$$

where $\rho^e + \rho^f = \rho^n$ is used in the second equality, and $\boldsymbol{m}^f = \boldsymbol{m}^n$ is used to derive the last equality. Following the definition of ϑ in (B.4) and $\hat{\alpha}_0$, $\hat{\alpha}_S$ in (4.13), we have

$$
\Delta t^2 \frac{\left\| \nabla p_K^{\tilde{e}} / \rho_K^e \right\|^2}{2\vartheta^2 e_K^n} = (\hat{\alpha}_0 \Delta t)^2 \frac{\left\| \nabla p_K^{\tilde{e}} / \rho_K^e \right\|^2}{2\hat{\alpha}_S^2 e_K^n} < 1,
$$

hence it follows that $\mathcal{G}\left(\boldsymbol{W}_2^\mu\right) > 0$, i.e., $\boldsymbol{W}_2 \in G$. □

References

[1] E. Audusse, F. Bouchut, M.-O. Bristeau, R. Klein and B. Perthame. A fast and stable well-balanced scheme with hydrostatic reconstruction for shallow water flows, SIAM Journal on Scientific Computing, 2004, 25: 2050-2065.

[2] J. Berberich, P. Chandrashekar, C. Klingenberg, and F. Röpke. Second order finite volume scheme for Euler equations with gravity which is well-balanced for general equations of state and grid systems. Communications in Computational Physics, 2019, 26(2): 599-630.

[3] J. Berberich, R. Käppeli, P. Chandrashekar and C. Klingenberg. High order discretely well-balanced methods for arbitrary hydrostatic atmospheres. Communications in Computational Physics, 2021, in press.

[4] A. Bermudez and M. E. Vazquez. Upwind methods for hyperbolic conservation laws with source terms. Computers & Fluids, 1994, 23: 1049-1071.

[5] N. Botta, R. Klein, S. Langenberg. Well-balanced finite volume methods for nearly hydrostatic flows. Journal of Computational Physics, 2004, 196(2): 539-565.

[6] J. Britton and Y. Xing. High order still-water and moving-water equilibria preserving discontinuous Galerkin methods for the Ripa model. Journal of Scientific Computing, 2020, 82(2): 1-37.

[7] F. Bouchut and T. M. De Luna. A subsonic-well-balanced reconstruction scheme for shallow water flows. SIAM Journal on Numerical Analysis, 2010, 48(5): 1733-1758.

[8] M. J. Castro and C. Parés. Well-balanced high-order finite difference methods for systems of balance laws. Journal of Scientific Computing, 2020, 82(2): 1-48.

[9] P. rashekar and C. Klingenberg. A second order well-balanced finite volume scheme for Euler equations with gravity. SIAM Journal on Scientific Computing, 2015, 37: B382-B402.

[10] P. Chandrashekar and M. Zenk. Well-balanced nodal discontinuous Galerkin method for Euler equations with gravity. Journal of Scientific Computing, 2017, 71(3): 1062-1093.

[11] A. Chertock, S. Cui, A. Kurganov, Ş. N. Özcan, and E. Tadmor. Well-balanced schemes for the Euler equations with gravitation: Conservative formulation using global fluxes. Journal of Computational Physics, 2018, 358: 36-52.
[12] B. Cockburn, S. Hou and C.-W. Shu. The Runge-Kutta local projection discontinuous Galerkin finite element method for conservation laws IV: The multidimensional case. Mathematics of Computation, 1990, 54: 545-581.
[13] B. Cockburn, S.-Y. Lin and C.-W. Shu. TVB Runge-Kutta local projection discontinuous Galerkin finite element method for conservation laws III: One-dimensional systems. Journal of Computational Physics, 1989, 84: 90-113.
[14] B. Cockburn and C.-W. Shu. TVB Runge-Kutta local projection discontinuous Galerkin finite element method for conservation laws II: General framework. Mathematics of Computation, 1989, 52: 411-435.
[15] B. Cockburn and C.-W. Shu. The Runge-Kutta local projection P1-discontinuous Galerkin finite element method for scalar conservation laws. ESAIM: Mathematical Modelling and Numerical Analysis, 1991, 25: 337-361.
[16] B. Cockburn and C.-W. Shu. The Runge-Kutta discontinuous Galerkin method for conservation laws V: Multidimensional systems. Journal of Computational Physics, 1998, 141: 199–224.
[17] E. Franck and L. S. Mendoza. Finite volume scheme with local high order discretization of the hydrostatic equilibrium for the Euler equations with external forces. Journal of Scientific Computing, 2016, 69: 314-354.
[18] J. M. Gallardo, C. Parés and M. J. Castro. On a well-balanced high-order finite volume scheme for shallow water equations with topography and dry areas. Journal of Computational Physics, 2007, 227(1): 574-601.
[19] D. Ghosh and E.M. Constantinescu. Well-balanced, conservative finite difference algorithm for atmospheric flows. AIAA Journal, 2016, 54(4): 1370-1385.
[20] S. Gottlieb, C.-W. Shu and E. Tadmor. Strong stability-preserving high-order time discretization methods. SIAM review, 2001, 43(1): 89-112.
[21] J. M. Greenberg and A. Y. LeRoux. A well-balanced scheme for the numerical processing of source terms in hyperbolic equations. SIAM Journal on Numerical Analysis, 1996, 33: 1-16.
[22] L. Grosheintz-Laval and R. Käppeli. High-order well-balanced finite volume schemes for the Euler equations with gravitation. Journal of Computational Physics, 2019, 378: 324-343.
[23] J.-L. Guermond, M. Nazarov and B. Popov. Second-order invariant domain preserving approximation of the Euler equations using convex limiting. SIAM Journal on Scientific Computing, 2018, 40: A3211-A3239.
[24] J.-L. Guermond, B. Popov and I. Tomas. Invariant domain preserving discretization-independent schemes and convex limiting for hyperbolic systems. Computer Methods in Applied Mechanics and Engineering, 2019, 347: 143-175.
[25] R. Käppeli and S. Mishra. Well-balanced schemes for the Euler equations with gravitation. Journal of Computational Physics, 2014, 259: 199-219.
[26] R. Käppeli and S. Mishra. A well-balanced finite volume scheme for the Euler equations with gravitation. The exact preservation of hydrostatic equilibrium with arbitrary entropy stratification. Astronomy & Astrophysics, 2016, 587: A94.
[27] C. Klingenberg, G. Puppo and M. Semplice. Arbitrary order finite volume well-balanced schemes for the Euler equations with gravity. SIAM Journal on Scientific Computing, 2019, 41(2): A695-A721.
[28] A. Kurganov. Finite-volume schemes for shallow-water equations. Acta Numerica, 2018, 27:

289-351.
[29] R. J. LeVeque. Balancing source terms and flux gradients on high-resolution Godunov methods: The quasi-steady wave-propagation algorithm. Journal of Computational Physics, 1998, 146: 346-365.
[30] R. J. LeVeque and D. S. Bale. Wave propagation methods for conservation laws with source terms, in Proceedings of the 7th International Conference on Hyperbolic Problems, 1998: 609-618.
[31] G. Li and Y. Xing. High order finite volume WENO schemes for the Euler equations under gravitational fields. Journal of Computational Physics, 2016, 316: 145-163.
[32] G. Li and Y. Xing. Well-balanced discontinuous Galerkin methods for the Euler equations under gravitational fields. Journal of Scientific Computing, 2016, 67: 493-513.
[33] G. Li and Y. Xing. Well-balanced finite difference weighted essentially non-oscillatory schemes for the Euler equations with static gravitational fields. Computers & Mathematics with Applications, 2018, 75(6): 2071-2085.
[34] G. Li and Y. Xing. Well-balanced discontinuous Galerkin methods with hydrostatic reconstruction for the Euler equations with gravitation. Journal of Computational Physics, 2018, 352: 445-462.
[35] C. Parés, C. Parés-Pulidob. Well-balanced high-order finite difference methods for systems of balance laws. Journal of Computational Physics, 2021, 425: 109880.
[36] C.-W. Shu. Bound-preserving high-order schemes for hyperbolic equations: Survey and recent developments. Theory, Numerics and Applications of Hyperbolic Problems II, Springer, Cham, 2018: 591-603.
[37] A. Thomann and M. Zenk. A second-order positivity-preserving well-balanced finite volume scheme for Euler equations with gravity for arbitrary hydrostatic equilibria. International Journal for Numerical Methods in Fluids, 2019, 89(11): 465-482.
[38] D. Varma and P. Chandrashekar. A second-order, discretely well-balanced finite volume scheme for Euler equations with gravity. Computers & Fluids, 2019, 181: 292-313.
[39] M. Veiga, D. A. Velasco-Romero and R. Abgrall. Capturing near-equilibrium solutions: A comparison between high-order discontinuous Galerkin methods and well-balanced schemes. Communications in Computational Physics, 2019, 26: 1-34.
[40] K. Wu and Y. Xing. Uniformly high-order structure-preserving discontinuous Galerkin methods for Euler equations with gravitation: Positivity and well-balancedness. SIAM Journal on Scientific Computing, 2021, 41(1): A472-A510.
[41] Y.Xing and C.-W. Shu. High order well-balanced WENO scheme for the gas dynamic equations under gravitational fields. Journal of Scientific Computing, 2013, 54(2): 645-662.
[42] Y. Xing and C.-W. Shu. High order finite difference WENO schemes with the exact conservation property for the shallow water equations. Journal of Computational Physics, 2005, 208: 206-227.
[43] Y. Xing and C.-W. Shu. High order well-balanced finite volume WENO schemes and discontinuous Galerkin methods for a class of hyperbolic systems with source terms. Journal of Computational Physics, 2006, 214: 567-598.
[44] Y. Xing, X. Zhang and C.-W. Shu. Positivity-preserving high order well-balanced discontinuous Galerkin methods for the shallow water equations. Advances in Water Resources, 2010, 33: 1476-1493.
[45] Y. Xing and C.-W. Shu. High order well-balanced WENO scheme for the gas dynamics equations under gravitational fields. Journal of Scientific Computing, 2013, 54: 645-662.
[46] Y. Xing and C.-W. Shu. A survey of high order schemes for the shallow water equations.

Journal of Mathematical Study, 2014, 47: 221-249.
[47] K. Xu, J. Luo and S. Chen. A well-balanced kinetic scheme for gas dynamic equations under gravitational field. Advances in Applied Mathematics and Mechanics, 2010, 2(2): 200-210.
[48] X. Zhang and C.-W. Shu. On positivity-preserving high order discontinuous Galerkin schemes for compressible Euler equations on rectangular meshes. Journal of Computational Physics, 2010, 229(23): 8918-8934.
[49] X. Zhang and C.-W. Shu. Positivity-preserving high order discontinuous Galerkin schemes for compressible Euler equations with source terms. Journal of Computational Physics, 2011, 230(4): 1238-1248.
[50] X. Zhang, Y. Xia and C.-W. Shu. Maximum-principle-satisfying and positivity-preserving high order discontinuous Galerkin schemes for conservation laws on triangular meshes. Journal of Scientific Computing, 2012, 50(1): 29-62.